Renewable and Sustainable Energy Reviews 175 (2023) 113186

Contents lists available at ScienceDirect

Renewable and Sustainable Energy Reviews

journal homepage: www.elsevier.com/locate/rser

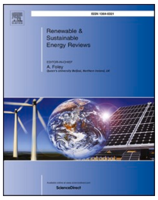

Entering new era of thermoelectric oxide ceramics with high power factor through designing grain boundaries

Cesar-Octavio Romo-De-La-Cruz [a], Yun Chen [a], Liang Liang [a], Sergio A. Paredes-Navia [a], Winnie K. Wong-Ng [b], Xueyan Song [a,*]

[a] Department of Mechanical and Aerospace Engineering, West Virginia University, USA
[b] Materials Measurement Science Division, National Institute of Standards and Technology, USA

ARTICLE INFO

Keywords:
Grain boundary
Thermoelectric
Seebeck
Oxide
Segregation
Dopant

ABSTRACT

Thermoelectric oxide ceramics could play a significant role in waste heat recovery using thermoelectric generators, accelerating clean energy generation and achieving net-zero emissions. In 2003, the thermoelectric performance of single-crystal $Ca_3Co_4O_{9+\delta}$ was evaluated with a dimensionless thermoelectric figure-of-merit (*ZT*) of 0.87. Polycrystalline $Ca_3Co_4O_{9+\delta}$ ceramics are typically only about 30% as efficient as single crystals since they have low electrical conductivity and low Seebeck coefficient. To improve the thermoelectric performance of polycrystalline $Ca_3Co_4O_{9+\delta}$, a unique approach was developed to drive dopants segregation at the grain boundaries to dramatically increase the Seebeck coefficient and electrical conductivity and total energy conversion efficiency of the oxide. This review exploited our pertinent results from five sets of dopants to elucidate that the grain boundary can be engineered to reverse their detrimental impact on electrical properties and provide the design domain to improve the electrical transport properties significantly. The approach to engineer the grain boundary can be used for the selection of dopants with the appropriate size that will ultimately result in oxide ceramics outperforming single-crystals. The present review unveils the atomic structure origin of the dopant segregation at grain boundaries and presents a feasible and valuable approach for treating the grain boundaries as a two-dimensional intergranular secondary phase complexion that is with magnitudes higher Seebeck coefficient than that of the intragrains. Such intergranular secondary phase complexion is independently tunable to decouple the strongly correlated physical parameters and simultaneously enhance the Seebeck coefficient, electrical power factor, and *ZT* over a broad temperature range.

1. Urgency to enhance the power factor of thermoelectric oxide ceramics

The global energy system has started the transition from fossil fuel to clean energy and hydrogen generation and consumption using natural gas power plants, nuclear power plants, turbine engines, concentrated solar power plants, and reversible solid oxide cells for electricity generation and hydrogen production. Nevertheless, for each of those systems, a total of up to 70% of the prime energy is heat that is usually unproductively released into the environment. For instance, power plants typically have roughly 60% of waste heat [1], whereas concentrating thermal power plants' conversion efficiency is currently releasing approximately 24% through radiator systems like those in vehicles [2]. In addition to the power generation systems, the industries that produce iron/steel and non-metallic minerals also release waste heat, especially at elevated temperatures, as high as 1273 K [3,4], while large-scale furnaces have high-temperature (up to 1673 K) discharges and offer the significant commercial potential for TE applications [5]. Many other industries generate waste heat from the exhaust and flue gas emissions, as well as heated air from heating systems [6], with high (922 K–1144 K) and ultra-high temperatures (>1144 K). As such, the waste heat recovery system market is forecast to exceed $70 billion by 2026.

Waste heat recovery utilizing thermoelectric (TE) power generators is one strategy to increase the sustainability of our electricity supply [7,8] or devices capable of directly converting temperature gradients into electricity (Fig. 1 a). Therefore, generating electricity utilizing waste heat with no additional CO_2 emissions is equivalent to generating electricity using renewable energy sources like solar and wind. TE converts thermal and electrical energy and provides a method for

---

* Corresponding author.
E-mail address: xueyan.song@mail.wvu.edu (X. Song).

https://doi.org/10.1016/j.rser.2023.113186
Received 27 July 2022; Received in revised form 9 January 2023; Accepted 12 January 2023

heating or cooling the materials. TE devices have no moving parts, are silent, and with maintenance-free operation. TE devices could enable a wide range of applications, from solid-state cooling to high-temperature power generation, and could dramatically increase the overall effectiveness of energy usage and reduce the use of fossil fuels [9–11].

However, the lack of effectiveness of TE materials in converting energy severely hampers the development of TE devices, which are desperately needed. For the majority of applications, TE technology has proven too inefficient to be economical [12,15–18]. The conversion efficiency of TE materials is characterized by the dimensionless figure-of-merit [19], *ZT*. *ZT* is defined as $S^2\sigma T/\kappa$, where S is the Seebeck coefficient, σ is the electrical conductivity, $S^2\sigma$ is the electrical power factor (*PF*), κ is the thermal conductivity, and T is the absolute temperature. The efficiency reaches about 10% when $ZT = 1$, and hence $ZT \geq 1$ is typically recognized as a requirement for practical applications. For TE materials to be capable of converting energy efficiently, the following three physical properties must be present simultaneously: (1) Low thermal conductivity κ, which permits a significant temperature differential between two ends of the materials; (2) High electrical conductivity σ, required for better carrier flow because it lowers internal resistance, and (3) Large Seebeck Coefficient S, which is thermomotive force that results in a high voltage [20]. However, because all three factors depend on carrier density, achieving high ZT is quite challenging, as shown in Fig. 1 [14], and they are linked and at odds in the following two ways [21,22]. First, the Seebeck coefficient is indirectly correlated with the carrier concentration n, but the electrical conductivity σ is directly correlated with the carrier concentration by $\sigma = ne\mu$, where μ is carrier mobility. When electrical conductivity is increased while carrier concentration is increased by doping, the Seebeck coefficient is simultaneously decreased, and the total power factor only marginally increases, as shown in Fig. 1c. Second, increasing carrier density increases the electrical contribution κ_{ele} to the thermal conductivity κ, as shown in Fig. 1d.

The strong interplay among those parameters limited the *ZT* to be ≈ 1 for various materials for many years until the 1990s when extensive nanostructure engineering [23,24] was used to improve the performance of TE materials. Nowadays, well-developed TE materials [25–28] have high *ZT* values, as shown in Fig. 1b [13].

Even though the performance of those materials is fascinating, they often have poor thermal or chemical stability and are toxic, heavy, and scarce as natural resources. Most of all, their application for high-temperature heat recovery is limited due to the strict requirement on the materials to demonstrate superior stability at high temperatures over an extended time. For those like SiGe [29] and $Yb_{14}MnSb_{11}$ [30] that do have superior stability, they can only operate in a rigorous oxygen-free atmosphere at high temperatures. Conversely, oxide ceramics are better suited for high-temperature applications because of their structural and chemical stability in the air. In contrast, oxide ceramics are typically not thought of as suitable TE application candidates because, in comparison to covalent alloys, they feature ionic bonding with a limited band. Low electrical conductivities are caused by the mobility and carrier concentrations, which are typically 100 to 1000 times smaller than in covalent materials.

1.1. *Uniqueness and barriers of $Ca_3Co_4O_{9+\delta}$ for TE application*

The excitement of TE oxide emerged after the unanticipated finding of significant thermopower in $Na_yCo_2O_4$ in 1997 and in $Ca_3Co_4O_{9+\delta}$ in 2000 [31–43]. The new series of oxides reported in the single crystal $Ca_3Co_4O_{9+\delta}$ [32], the single crystal $Na_yCo_2O_4$ [34], and more importantly for the addition of dopants in bulk $Ca_3Co_4O_{9+\delta}$ with Bi [31], Sr [39], Mg [39], SrBi [39], Na [40], and Cd [43] showed the potential of

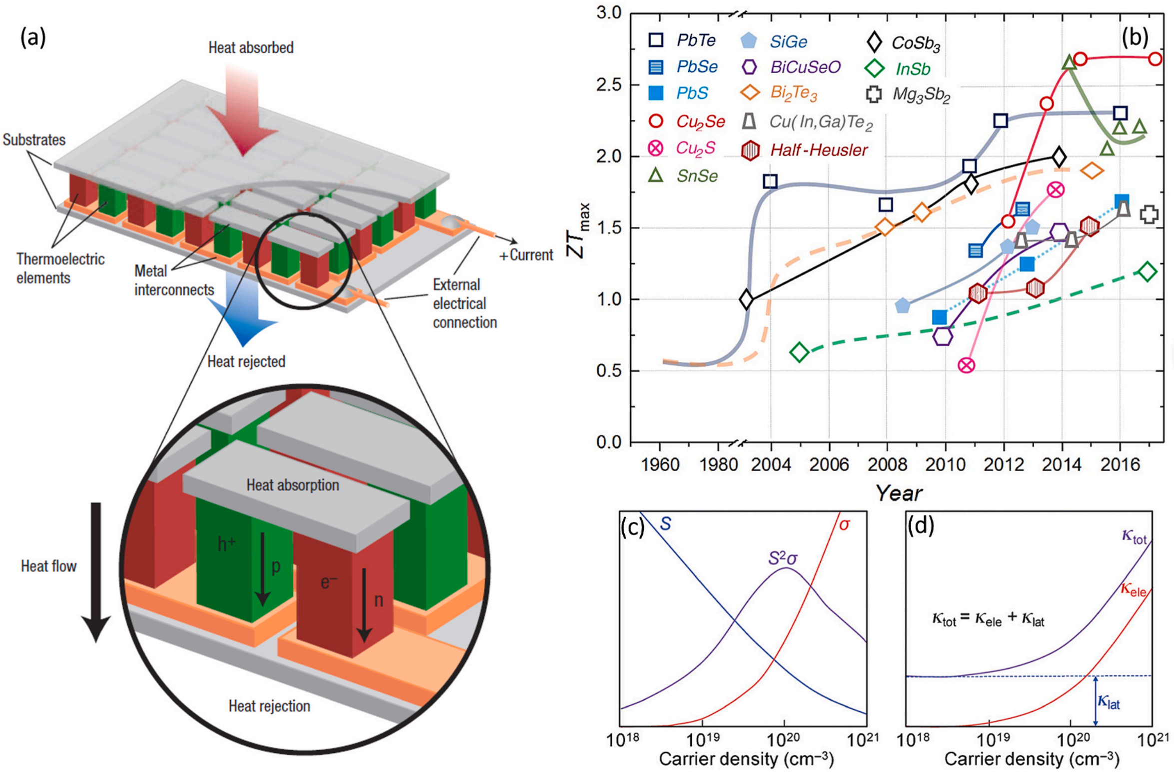

Fig. 1. (a) Thermoelectric module for both cooling (with an applied external power supply) and electricity generation (with an applied external heat source) [12]. (b) Established TE materials developed over the last decades and their maximum ZT. These state-of-the-art thermoelectric materials often suffer from poor thermal or chemical stability at elevated temperatures in air [13]. From Science 357, eaak9997 (2017). Reprinted with permission from AAAS. (c) & (d)The strong interplay between physical parameters related to thermoelectric properties of the material, where the carrier density influence *S*, *σ*, and κ_{ele} [14]. © 2015 WILEY-VCH Verlag GmbH & Co. KGaA, Weinheim.

these new series of oxide materials as TE materials. The low thermal conductivity and high *PF* were achieved simultaneously in the unit cell level of $Ca_3Co_4O_{9+\delta}$, due to the presence of two subsystems with entirely dissimilar physical characteristics. As shown in Fig. 2, an incommensurate character in the $Ca_3Co_4O_{9+\delta}$ monoclinic crystal structure [44] is explicitly described as $[Ca_2CoO_3]_{b1}/[CoO_2]_{b2}$, where b_1 and b_2 are two distinct periodicities along the *b* axis for the rock salt type Ca_2CoO_3 subsystem and the CoO_2 subsystem respectively. The electrically conductive CoO_2 sheets have a strongly correlated electron system that serves as electronic transport layers, while insulating rock-salt-type Ca_2CoO_3 misfit layers serve as phonon scattering centers for decreasing thermal conductivity. In 2003, a *ZT* of 0.87 at 973 K [32] was published for $Ca_3Co_4O_{9+\delta}$ single-crystals, rendering this inexpensive, lightweight, and non-toxic $Ca_3Co_4O_{9+\delta}$ one of the best candidates for *p*-type TE oxide since then. However, it is the misfit-layered structure that immediately brings another critical barrier to practical application. The $Ca_3Co_4O_{9+\delta}$ single-crystal shows significant anisotropic electrical activity due to the two-layered structure. Temperature-dependent electrical conductivity [45] measurements in directions perpendicular and parallel to the *ab* plane of the unit cell reveal that the former is 500–1000 times less than the latter. As a result, two-dimensional properties pose a significant obstacle to the development of high-performance polycrystalline devices. It is necessary to produce polycrystalline $Ca_3Co_4O_{9+\delta}$ ceramics in a way that simultaneously encourages densification and crystal texture.

Improving the TE performance of $Ca_3Co_4O_{9+\delta}$ ceramics using various approaches further encountered the following challenges. *(1) Limitation of rendering crystal texture of pristine $Ca_3Co_4O_{9+\delta}$ in increasing the electrical conductivity:* Special fabrication methods such as hot-pressing [46], cold high-pressure pressing [47,48], magnetic alignment [49], and spark plasma sintering process (SPS) were widely employed to produce the polycrystal samples with crystal alignment. However, the highly textured pristine $Ca_3Co_4O_{9+\delta}$ are typical with the peak *ZT* [19,50,51] of 0.2–0.3, which is only ≈30% of what is predicted for single-crystals. *(2) Limitation of using cation substitutions in the lattice in improving the electrical power factor:* Compared to single-crystal cobaltite, polycrystalline cobaltite has a lower thermal conductivity *κ*, which ranges from ≈2 to 3 $W\ m^{-1}K^{-1}$. Low *S* and high electrical resistivity *ρ* are the primary causes of the polycrystalline $Ca_3Co_4O_{9+\delta}$ poor *ZT* value, which also contributes to a comparatively low electrical power factor. A lot of research has previously been done on stoichiometric substitution at the Ca and/or Co sites utilizing different metals [45,52]. Nevertheless, similar to other TE materials, since both Seebeck coefficient and electrical conductivity are dependent on carrier concentration, conventional doping for improving the carrier concentration often causes an increase in electrical resistivity while simultaneously lowering the Seebeck coefficient, which ultimately results in a relatively little rise in the total power factor. (3) *The barrier to introducing nano-inclusions for reducing thermal conductivity:* Nano-inclusions have been widely proven to be effective in reducing the thermal conductivity of different TE materials. However, for $Ca_3Co_4O_{9+\delta}$, only very few elements were identified to be able to form nano-inclusions without reacting with Ca or Co, or substituting Ca or Co in the lattice as dopants. Even the Ag inclusion was attempted [53,54] due to the fast agglomeration of Ag during the high-temperature sintering, and the Ag inclusions are as big as ≈500 nm, and not dense enough to effectively scatter the photons at different frequency ranges. (4) *Limitation in the synthetic approach of combining defects for increasing the overall ZT:* Finally, the combination of SPS for rendering the crystal texture, Lu doping in the lattice, and the Ag nano-inclusion were simultaneously utilized to increase the peak *ZT* value to 0.61 [45], which is still significantly lower than what is expected from the single-crystal and not viable for practical applications.

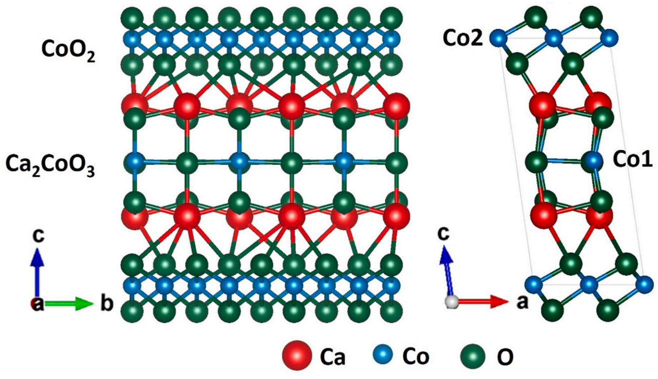

Fig. 2. The unit cell structure of $Ca_3Co_4O_{9+\delta}$ showing the alternating subsystems of electrically conductive CoO_2 sheets and insulating rock-salt-type Ca_2CoO_3 layers.

1.2. *Scrutiny to engineer grain boundaries of TE $Ca_3Co_4O_{9+\delta}$ ceramics*

It is worthwhile to point out that among the various methods for enhancing the performance of oxide ceramics, the GB structure in $Ca_3Co_4O_{9+\delta}$ ceramics is barely studied and poorly understood. The transport properties of pristine single-crystals and polycrystalline materials, such as those from $SrTiO_3$, revealed that electrical conductivity was heavily affected by the GBs [55]. In contrast, the Seebeck Coefficient of the polycrystalline sample is typically not dominated by the GB. The Seebeck coefficients of the polycrystalline ceramics present the same behavior as the single crystals. This phenomenon is also shared by the pristine $Ca_3Co_4O_{9+\delta}$ ceramics. We have demonstrated that the pristine $Ca_3Co_4O_{9+\delta}$ ceramics are sintered at different temperatures and possess different grain sizes and different GB densities, and the electrical conductivity changes dramatically while the Seebeck coefficient remains intact and constant at the different temperature regimes [56]. In terms of doping, the predominant model for the GB region of various thermoelectric materials predicts that GBs should have a minimal impact on the mobility at high doping levels, but in fact, the carrier mobility is frequently significantly decreased.

Traditionally, for various ceramics, the thermoelectric properties might be enhanced by decreasing the effect of GBs on electron transport and by reducing the abundance and misorientation angles of the GBs. For the $Ca_3Co_4O_{9+\delta}$ ceramics with large significant anisotropy, when the high angle GBs, (with *c*-axis misorientation of 45–90°) could be largely avoided by rendering the formation of the crystal texture during processing, the low angle GBs, (with a misorientation angle of 1–30°), dominate the well-textured bulk samples even for the samples processed using the special techniques such as spark plasma sintering (SPS). To make the oxide ceramics viable to the large-scale application, it is mandatory to develop the ceramics processing that promotes crystal texture formation using conventional materials processing, including cold-pressing and subsequent sintering. Furthermore, the GBs, especially the low angle GBs, are not avoidable for polycrystalline ceramics. Ideally, a feasible approach of simultaneously improving the crystal texture and turning the detrimental GBs into the conducting pathways to improve the thermoelectric performance is ultimately desired.

Based on the above, the authors have strived to understand the impact of nanostructure engineering, especially tailoring the dopants segregation at GBs to control the crystal texture and the TE performance of $Ca_3Co_4O_{9+\delta}$ ceramics. As for all other ceramics [57,58], when the crystals are with dopants, in addition to altering the intragranular chemistry, the dopants could segregate at the GBs [59]. The dopant segregation at the GBs has a major impact on the materials processing since the ionic diffusion along the GBs drives the grain development, phase alteration occurring during the solid-state sintering reactions, and crystallographic texture development that affects the carrier mobility, especially for the polycrystalline ceramics from $Ca_3Co_4O_{9+\delta}$ that possess large anisotropy at the unit cell and single-crystal levels, and heavily depending on the GB structure. In electroceramics, dopants segregation at the GBs could further render the creation of the space-charge layer next to the GB plane and cause the solutes and defects to be distributed differently within the grain interiors [60,61] thus affecting the carrier density and the Seebeck coefficient that is characteristics of carrier concentration and believed to be an intrinsic property of materials with fixed chemistry.

For $Ca_3Co_4O_{9+\delta}$ oxide ceramics, Ag at GBs in $Ca_3Co_4O_{9+\delta}$/Ag composite was deemed as facilitate GB sliding and enhance grain orientation during sintering and provide phonon scattering to reduce thermal conductivities [53,54,62,63]. Beyond that, the atomic structure and chemistry of GB itself in $Ca_3Co_4O_{9+\delta}$ ceramics is barely studied and poorly understood. While the GBs might have a detrimental impact on carrier mobility, they can also, especially those associated with the dopants segregation and different chemistry from that of grain interior, have a good impact in both reducing the thermal conductivity and improving the electrical transport properties.

For $Ca_3Co_4O_{9+\delta}$, the scope to which point defects might segregate to the GBs, the methods for precisely introducing dopants to segregate at the GBs, and the impact of dopants GBs segregation on the performance was not studied. The authors firmly believe that the transport properties are greatly affected by the enrichment or depletion of dopants at the GBs and the ensuing redistribution of mobile charge carriers nearby the GBs; for example, they act as carrier filtering and increase the Seebeck coefficient. To better understand the possible dopants GB segregation and, most importantly, the intrinsic source for the dopant segregation and how it affects TE performance, especially the Seebeck coefficient and electrical power factor, the authors studied various sets of dopants on nanostructure and the thermoelectric performance of $Ca_3Co_4O_{9+\delta}$ based oxide ceramics. In the following sections, the authors reviewed the thermoelectric performance and the structure of ceramics incorporating five sets of dopants with different valence states, different ionic sizes, and significant variations in mass. Those five sets of dopants include single dopants of monovalent potassium K^+, divalent Ba^{2+}, trivalent Bi^{3+}, dual dopants of divalent Ba^{2+}, trivalent Bi^{3+}, as well as dual dopants of Bi^{3+} and Tb^{3+}. The ceramics with five sets of different dopants constantly and consistently demonstrate the improvement of the crystal texture and, surprisingly, simultaneous increase of the electrical conductivity and Seebeck coefficient. Using the conventional sol-gel chemical processing of the precursor powders, standard cold pressing, and sintering for the $Ca_3Co_4O_{9+\delta}$ system with up to two dopants [52,56,64–71], the authors have demonstrated the resultant improved peak *ZT* to 0.9, thus significantly outperform $Ca_3Co_4O_{9+\delta}$ single crystals. Such high performance of polycrystalline $Ca_3Co_4O_{9+\delta}$ with ZT of 0.9 is achieved by increasing the electrical power factor, $S^2\sigma$, (up to a factor of ≈4.6 at 310 K and ≈2.3 at 1073 K) rather than the reduction of thermal conductivity that is largely achieved in various thermoelectric materials through nanostructure engineering. We identified the atomic structure origin of the crystal texture development and the simultaneous increase of the Seebeck coefficient induced by doping. We further discussed the implication of this part of the work on engineering polycrystalline ceramics. Throughout this review paper, readers are referred to the respective original articles for information on measurement uncertainties.

2. Dopants GB segregation for increasing *Seebeck Coefficient* and *conductivity*

In terms of ceramic materials processing, as stated previously, due to the significant anisotropy in the electrical transport properties of $Ca_3Co_4O_{9+\delta}$ single crystals, it is essential to sinter polycrystalline $Ca_3Co_4O_{9+\delta}$ bulk ceramics in a way that simultaneously encourages densification and crystal texture. Instead of using special techniques such as SPS, traditional cold pressing and sintering to create oxide pellets utilizing the chemical sol-gel route-generated powders to guarantee the ideal stoichiometry and uniform distribution of the dopants were used. The calcined powders could be with a grain size of ≈100 nm. During the sintering of the pressed pellets, there is significant grain growth to a grain size over ≈2 μm, thus densifying the pellets, and promoting crystal texture. Upon controlled calcination, pellet pressing pressure, sintering temperature, and sintering atmosphere, the authors have successfully demonstrated that the *ZT* of the pristine $Ca_3Co_4O_{9+\delta}$ polycrystal samples synthesized through the above-mentioned conventional sintering is with a peak *ZT* of ≈0.28, approaching the best reported pristine $Ca_3Co_4O_{9+\delta}$ synthesized using SPS [72,62]. Those well-excised processing procedures for making the $Ca_3Co_4O_{9+\delta}$ ceramics have been consistently adapted to conduct the samples with different chemistry presented in this review. The common approaches for each of the samples include: (1) *electrical and thermal properties measurement* using the commercially available standard "Seebeck and Electrical Resistivity Measurement System" and "Laser Flash Analyzer"; (2) *crystal texture and nanostructure characterization* using X-ray diffraction (XRD), scanning electron microscopy (SEM), and transmission electron microscopy (TEM); (3) *atomic structure and chemistry analysis* of dopants distribution in the lattice and at the GBs using Z-contrast imaging, Electron Energy Loss Spectroscopy (EELS), and Energy Dispersive Spectroscopy (EDS).

2.1. *Single dopants monovalent K^+ segregation at GBs*

The non-stoichiometric addition of the low mass potassium on the nanostructure and thermoelectric performance of $Ca_3Co_4O_{9+\delta}$ ceramics has been studied (see Fig. 3). The samples had the intended composition of $Ca_3Co_4O_{9+\delta}K_x$ (x = 0, 0.05, 0.1, 0.15, and 0.2). The nano lamellas with *c*-axis fiber texture are present in all $Ca_3Co_4O_{9+\delta}$ grains with or without dopants [52]. The nanostructure and chemical analysis exposed the segregation of K at the $Ca_3Co_4O_{9+\delta}$ GBs between two crystal grains with different c-axis. In contrast, the $Ca_3Co_4O_{9+\delta}$ grain interior was free of K. There is no formation of the nanoscale secondary phase at the GBs due to the K segregation. The K is presumably present as the solid solution at the GBs.

At the best doping concentration, potassium GB segregation decreased electrical resistivity while concurrently improving the Seebeck coefficient, which led to a significant improvement in power factor. The sample $Ca_3Co_4O_{9+\delta}K_{0.1}$ attained a power factor of 0.93 mW K^{-2} m^{-1} at 320 K, which is 126% increase from pure $Ca_3Co_4O_{9+\delta}$.

Furthermore, compared to pristine $Ca_3Co_4O_{9+\delta}$, the resistivity of the $Ca_3Co_4O_{9+\delta}K_{0.1}$ sample is much lower. The distinct dopants monovalent K^+ segregate at the GBs only while leaving the grain interior free of substitution of dopants. This is presumably due to the large ionic size difference between the dopants K^+ (152pm) and the host Ca^{2+} (114pm) and $Co^{3+/4+}$ (≈80pm). Accelerated grain growth and the formation of the crystal texture were produced by the segregation of these large ions to the GBs. The simultaneous improvement in S represents the most significant performance change, indicating the decreased carrier density.

2.2. *Single dopants divalent Ba^{2+} segregation at GBs*

This phenomenon of having oversized dopants segregation to the GB is repeated for divalent Ba^{2+}. In the sample of $Ca_3Co_4Ba_xO_{9+\delta}$, as shown in Fig. 4, using EDS analysis under TEM, in stark contrast to the grain interior that is free of Ba, there is a strong Ba signal detected from the GB region. Ba appears to be present as the solid solution enriched at the GB region only, and no nanoscale secondary phase, either amorphous or crystalline [73], was observed at the Ba-enriched $Ca_3Co_4Ba_xO_{9+\delta}$ GBs.

While the individual crystal from the $Ca_3Co_4Ba_{0.05}O_{9+\delta}$ sample presents a similar dimension and anisotropy aspect ratio to that of the pristine $Ca_3Co_4O_{9+\delta}$ sample, Ba segregation at GBs is sufficient enough to densify the bulk materials and render the grain alignment. Such a strong crystal texture significantly increases the carrier mobility and reduces the electrical resistivity (Fig. 4a -Bottom). Furthermore, the non-stoichiometric introduction of a slight amount of Ba causes a substantial

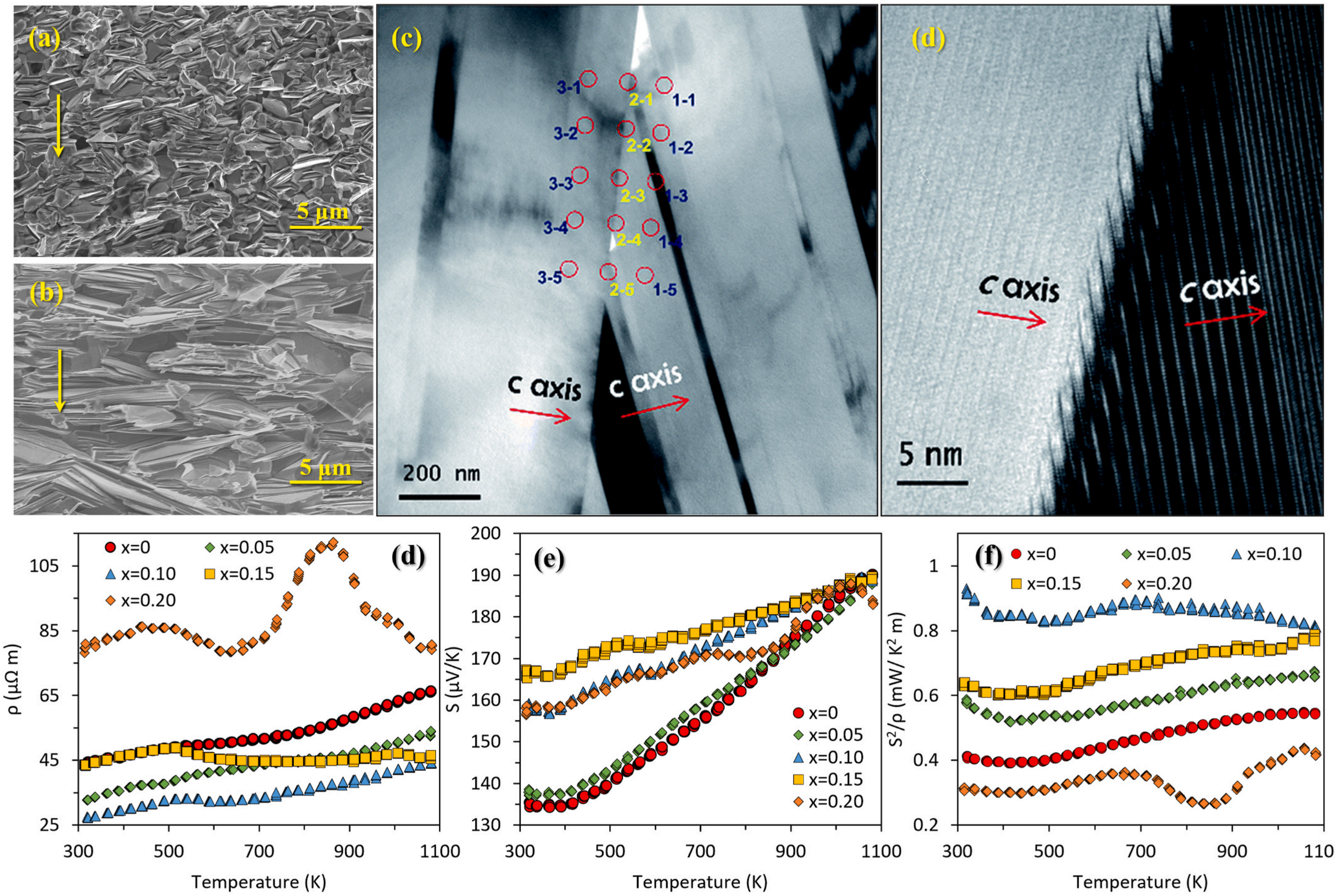

Fig. 3. Cross-sectional SEM images from the fractured surface after sintering of (a) $Ca_3Co_4O_{9+\delta}$ and (b) $Ca_3Co_4O_{9+\delta}K_{0.1}$ exhibit how the grain boundary segregation of the K dopant boost the alignment and grain growth on the material. TEM images of the $Ca_3Co_4O_{9+\delta}K_{0.1}$ sample showing the (c) GB from crystals with various *c* axis orientations. (d) HRTEM image of the GB displaying that K segregation does not promote the formation of a secondary phase at nanoscale. Temperature dependence of electrical properties for $Ca_3Co_4O_{9+\delta}K_x$: (e) ρ, (f) S, and (g) $S^2\sigma$. Improvement in power factor for best doping concentration, $Ca_3Co_4O_{9+\delta}K_{0.1}$, attained a 126% increase from pure $Ca_3Co_4O_{9+\delta}$. Reproduced from Sustainable Energy Fuels, 2018,2, 876–881, with permission from the Royal Society of Chemistry.

improvement in the Seebeck coefficient S and thermoelectric performance of calcium cobaltite $Ca_3Co_4O_{9+\delta}$ ceramics. At 323 K, S of $Ca_3Co_4O_{9+\delta}$ is 135 μV K^{-1}, while S of $Ca_3Ba_{0.05}Co_4O_{9+\delta}$ is 162.5 μV K^{-1}. The S for $Ca_3Ba_{0.05}Co_4O_{9+\delta}$ sample increases as the electrical resistivity ρ decreases, leading to a high power factor of 843 μW m^{-1} K^{-2} at 1007 K. The impact of the addition of Ba^{2+} can be consistently interpreted as the acts of a carrier filtering barrier layer in the $Ca_3Co_4O_{9+\delta}$ GBs that leads to a decrease of the carrier concentration and increased Seebeck coefficient (Fig. 4b -Bottom).

2.3. *Single dopants trivalent Bi^{3+} intragranular solubility and segregation at GBs*

Segregation of Ba^{2+} or K^+ at GBs is apparently due to the significant difference in ionic radius compared to the $Ca_3Co_4O_{9+\delta}$ lattice sites. Ca^{2+} and Co^{2+}/Co^{3+} are with a radius of 114 p.m. and 80 p.m., respectively, while the ionic radius for Ba^{2+} and K^+ are 149 p.m. and 152 p.m. As a result, rather of the Coulomb interaction, the lattice strain effect resulting from the ionic size difference is hypothesized to be the main factor behind the dopants GB segregation. However, the concentrations of dopants at GBs may differ from their bulk values, depending on the sign and magnitude of their charge, as well as the exact ionic size of the dopants. In the sample $Ca_{2.7}Bi_{0.3}Co_4O_{9+\delta}$, Bi is selected as dopant because Bi^{3+} substitution of Ca^{2+} could incorporate one electron per cation dopant and reduce the concentration of the majority carrier, although the precise amount of the lowered carrier concentration is dependent on other factors such as oxygen vacancies. This is line with the experimental findings in Fig. 5b, which demonstrate the improved S resulting from the reduced carrier concentration at both the low and high-temperature regimes. The somewhat larger trivalent dopants of Bi^{3+}, with the ionic radius of 117 p.m., have intragranular solubility while possessing segregation at GBs [67], shown in Fig. 5.

2.4. *Dual dopants of Ba^{2+} with Bi^{3+} and competing dopants segregation at GBs*

It is worthwhile to point out that both the K and Ba were introduced using non-stoichiometry addition of $Ca_3Co_4K_xO_{9+\delta}$ and $Ca_3Co_4Ba_xO_{9+\delta}$, respectively. While the dopants were segregated at the GBs only, the intragranular chemistry remained consistent with the stoichiometry of $Ca_3Co_4O_{9+\delta}$. In the case of Bi, it is one of the earliest doping elements to be used to replace Ca and has been widely studied since the year 2006 [74,75]. However, all of the investigations were on samples with designed stoichiometry. The Bi segregation at GBs in those $Ca_{3\text{-}x}Bi_xCo_4O_{9+\delta}$ samples was not reported until the year 2016 in our study. In the $Ca_{3\text{-}x}Bi_xCo_4O_{9+\delta}$ sample, the Bi segregation at GBs has apparently caused the intragranular chemistry to diverge from the intended stoichiometry.

Such intragranular chemistry deviation due to the Bi grain boundary segregation was restored by applying dual dopants of Bi^{3+} and Ba^{2+} with different oxidation valence states. The polycrystalline material system is intended to have a nominal chemistry of $Ca_{3-x}Bi_xBa_yCo_4O_{9+\delta}$ with

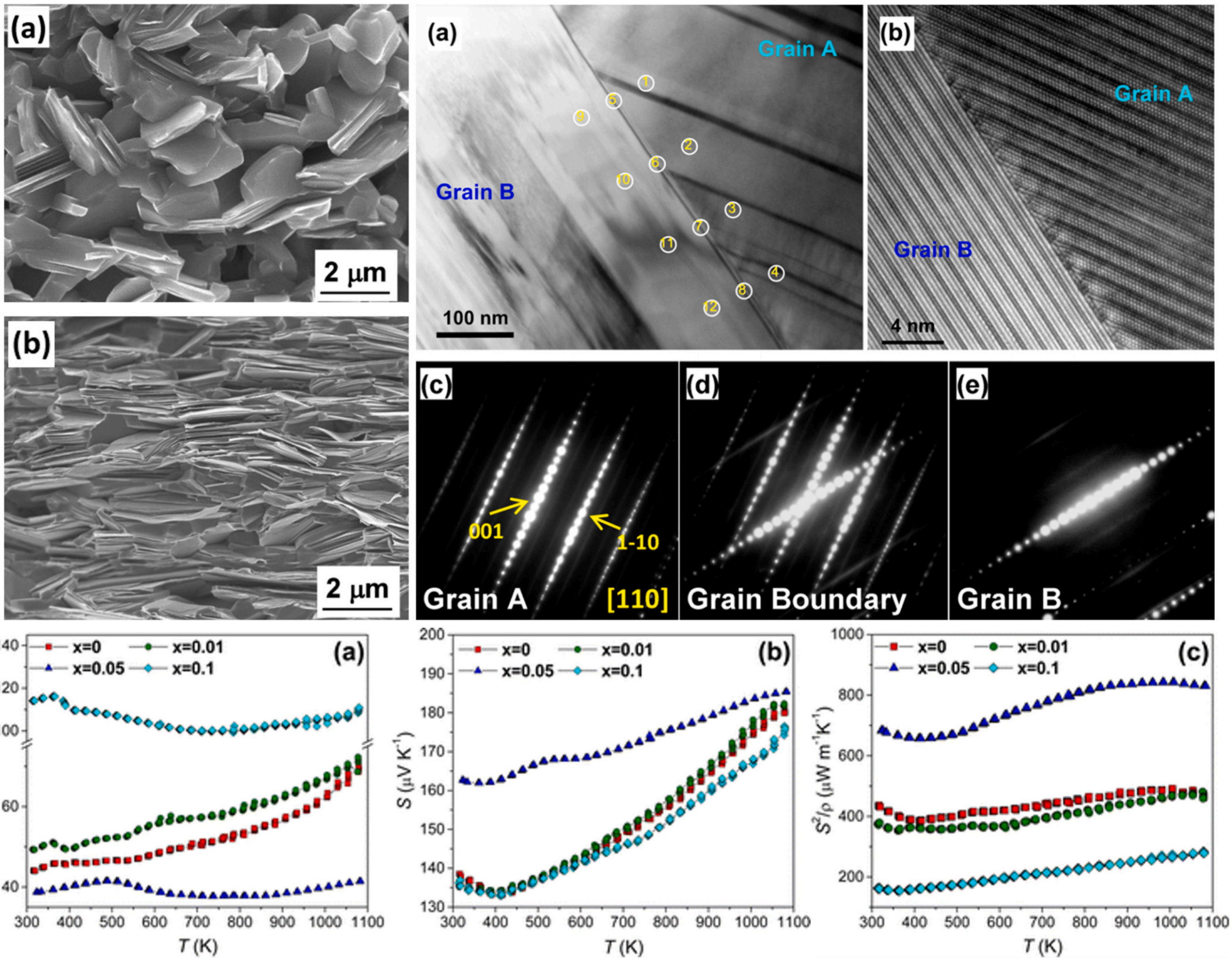

Fig. 4. Top left: Cross-sectional SEM images from the fractured surface of the samples displaying the improved crystal texture of the samples with Ba doping compared to baseline in (a) $Ca_3Co_4O_{9+\delta}$ and (b) $Ca_3Ba_{0.05}Co_4O_{9+\delta}$. **Top right:** Nanostructured analysis of $Ca_3Ba_{0.05}Co_4O_{9+\delta}$ samples. (a) TEM image displaying two $Ca_3Co_4O_{9+\delta}$ grains. (b) HRTEM image displaying the $Ca_3Co_4O_{9+\delta}$ GB free of the secondary phase. Electron diffraction patterns were obtained from grain A(c), from the GB area between grains A and B(d), and from grain B(e). **Bottom:** Electrical properties for the $Ca_3Ba_xCo_4O_{9+\delta}$ samples as a function of temperature. (a) ρ; (b) S; and (c) $S^2\sigma$. Reprinted (adapted) with permission from {Inorg. Chem. 2015, 54, 18, 9027–9032}. Copyright {2015} American Chemical Society.

concurrent stoichiometric substitution of Bi for Ca and non-stoichiometric addition of trace quantities of Ba. In the samples with dual dopants, it surprisingly demonstrated the Bi depletion from the GB with the indication of re-establishment of intragranular stoichiometry. On the other hand, accompanying the Bi depletion at the GB, is significant Ba segregation at the GB alone without the Ba incorporation into the lattice (as presented in Fig. 6).

Apparently, there is competing dopants segregation that reveals very important mechanisms that could contribute to the segregation's driving force. Whenever Bi is the sole dopant in $Ca_3Co_4O_{9+\delta}$, the Bi segregation at the GBs is accompanied by the Bi intragranular solubility. This Bi segregation could be the result of the mechanical strain relaxation effect or electrical Coulomb interactions. This latter effect may become dominant when the doping ions and host ions slightly differ in size. Ca^{2+} has an ionic radius of 114 p.m., while Bi^{3+} has an ionic radius of 117 p.m., which is slightly larger than Ca^{2+}. Due to the similar ionic radius of Bi^{3+} and Ca^{2+}, it is difficult to determine exactly what drives Bi^{3+} segregation. In contrast, the ionic radius of Ba^{2+} is 149 p.m., and significantly larger than that of Ca^{2+} and Bi^{3+}.Further, Ba can be introduced with no extra charge because it has the same valence state as Ca. In the case of the GBs, the segregation of Ba and ion-size mismatch between impurities and host ions results in elastic strain due to the simultaneous segregation of Ba and depletion of Bi. Accordingly, on the basis of the differing ion radii of two segregant ions, such a segregant competing phenomenon may be explained. The GBs of $Ca_3Co_4O_{9+\delta}$ ceramics attract oversized cations [68]. As far as we are aware, our research is the first to demonstrate competitive dopant segregation at GBs from TE ceramics and other oxides.

At the fixed Bi substitution level, there is a continuous increase of S due to Ba addition. It is worthwhile to point out that the $Ca_3Co_4Ba_xO_{9+\delta}$ with dual dopants presents a different Seebeck temperature dependence than that of samples with Bi or Ba doping alone. For the samples with Bi substitution, the doping increases the S at both the low and high-temperature regimes. For the samples with Ba non-stoichiometric addition, the Ba segregation at the GBs significantly raises the S at the low-temperature regime, and the increment gradually decreases with the increase of the temperature and completely diminishes at 1073 K. In comparison with the baseline and the sample with the single dopants, the total Seebeck coefficient of the sample with dual dopants of both Ba and Bi is approximately a weighted sum of the increase of the Seebeck coefficient induced by a single dopant. Most importantly, the selective dopants spatial distribution of having one dopant of Bi incorporation in

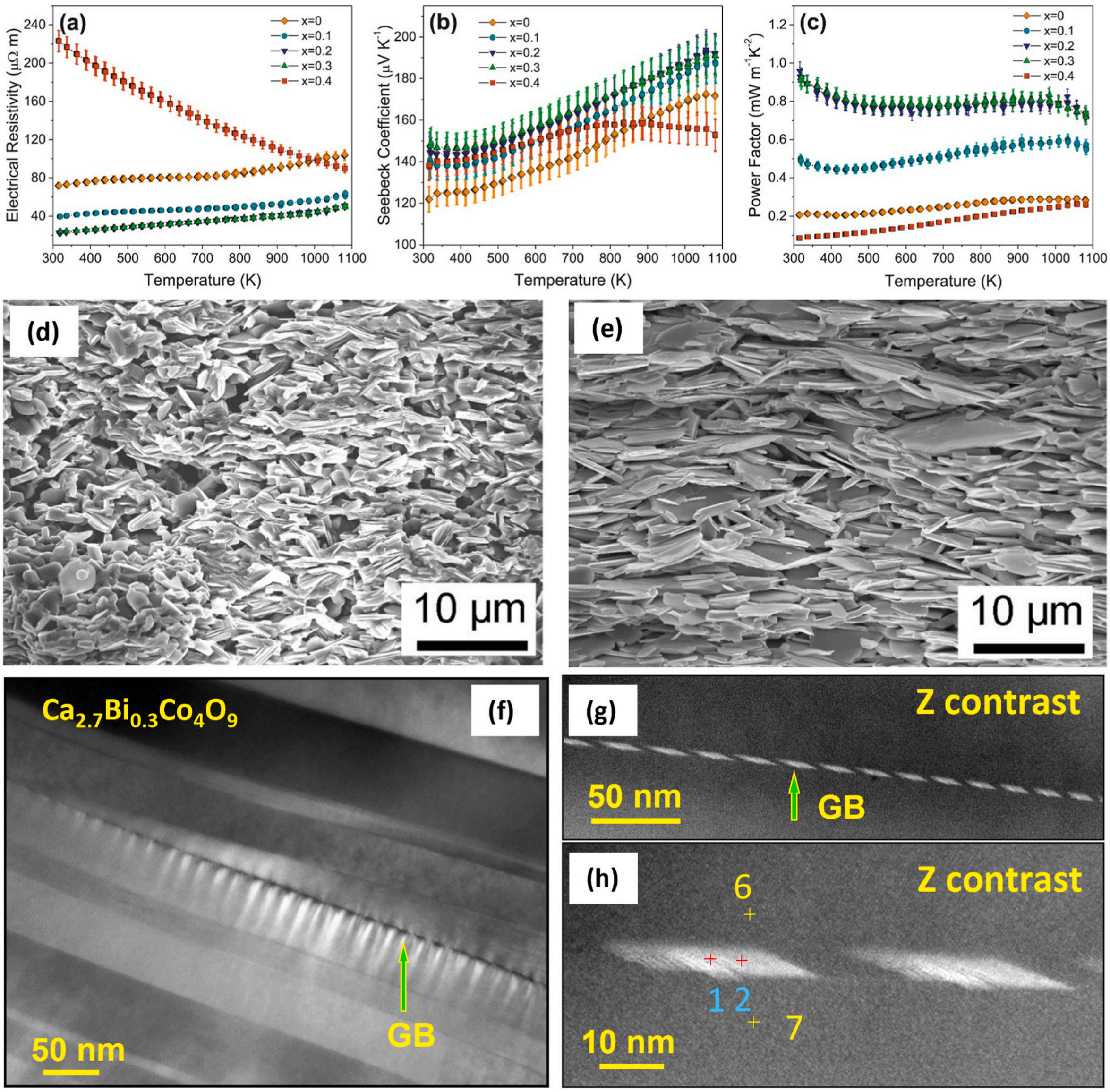

Fig. 5. Temperature dependence of the electrical properties of $Ca_{3-x}Bi_xCo_4O_{9+\delta}$: (a) ρ, (b) S, and (c) $S^2\sigma$, Bi segregation increases the S while reducing the ρ. Crystal texture development can be observed for the Bi doping as shown with the SEM cross-sectional images for (d) $Ca_3Co_4O_{9+\delta}$ and (e) $Ca_{2.7}Bi_{0.3}Co_4O_{9+\delta}$. Nanostructure images of $Ca_{2.7}Bi_{0.3}Co_4O_{9+\delta}$: (f) TEM image displays characteristic GB and neighboring grains with misorientation angle ~6°, (g) STEM Z-contrast image from the same GB as shown in (f), and (h) high magnification STEM Z-contrast image of the same GB shown in (g), displaying two segregation sites. Reprinted from Journal of the European Ceramic Society 36 (2106) 601–607, Copyright (2016), with permission from Elsevier.

the $Ca_3Co_4Ba_xO_{9+\delta}$ lattice, while another dopant of Ba segregation at the GB, provides an excellent opportunity for us to separately tune the electrical performance of grain and GBs and decouple the Seebeck coefficient and electrical conductivity and increase both simultaneously over a wide temperature range.

2.5. *Dual dopants of Bi^{3+} and Tb^{3+} with intragranular substitution and segregation at GBs for outperforming single crystals*

While the oversized dopants are found to segregate at the GBs consistently, it is worthwhile to investigate the effect of the undersized dopants, such as that rare-earth element Tb that is with an ionic radius significantly smaller than that of the Ca. Doping rare earth elements was consistently reported to decrease the hole concentrations in $Ca_3Co_4O_{9+\delta}$ and led to an increase in both the Seebeck coefficient and electrical resistivity [76–79]. However, the influence of the rare earth element doping on the microstructure and GB structure has not been systematically reported. In our work, it is identified that in $Ca_3Co_4Ba_xO_{9+\delta}$ samples with Tb substitution of Ca, the rare earth element Tb retards the grain growth. Under the same sintering conditions used for pristine $Ca_3Co_4O_{9+\delta}$, the grain size of $Ca_{2.5}Tb_{0.5}Co_4O_{9+\delta}$ sample is ≈50% of that of $Ca_3Co_4O_{9+\delta}$. The dopant Tb may have increased the onset of the minimum required temperature to promote the anisotropy growth during sintering [80] and/or lowered cation diffusivity along the GBs. It is also interesting to notice that Tb is depleted at the GBs, while the nanostructure at the GBs presents no apparent changes except for the lattice distortion. Complementary to our hypothesis of oversized dopants segregated to the GBs, this result on the single Tb dopant further demonstrated that undersized dopants, such as Tb, are depleted at the GB because the ionic radius of Tb^{3+} and Tb^{4+} is 106 p.m. and 90 p.m., respectively, and less than that of Ca^{2+} (114 p.m.).

To compensate the Tb and related cation deficiency at GBs, the Bi–Tb dual dopants approach was attempted. Instead of using Bi substitution, the Bi-non-stoichiometric addition was applied to this set of samples with the designed chemistry of $Ca_{2.95}Tb_{0.05}Co_4O_{9+\delta}Bi_x$.

The dual dopants promote crystal texture formation and consistently

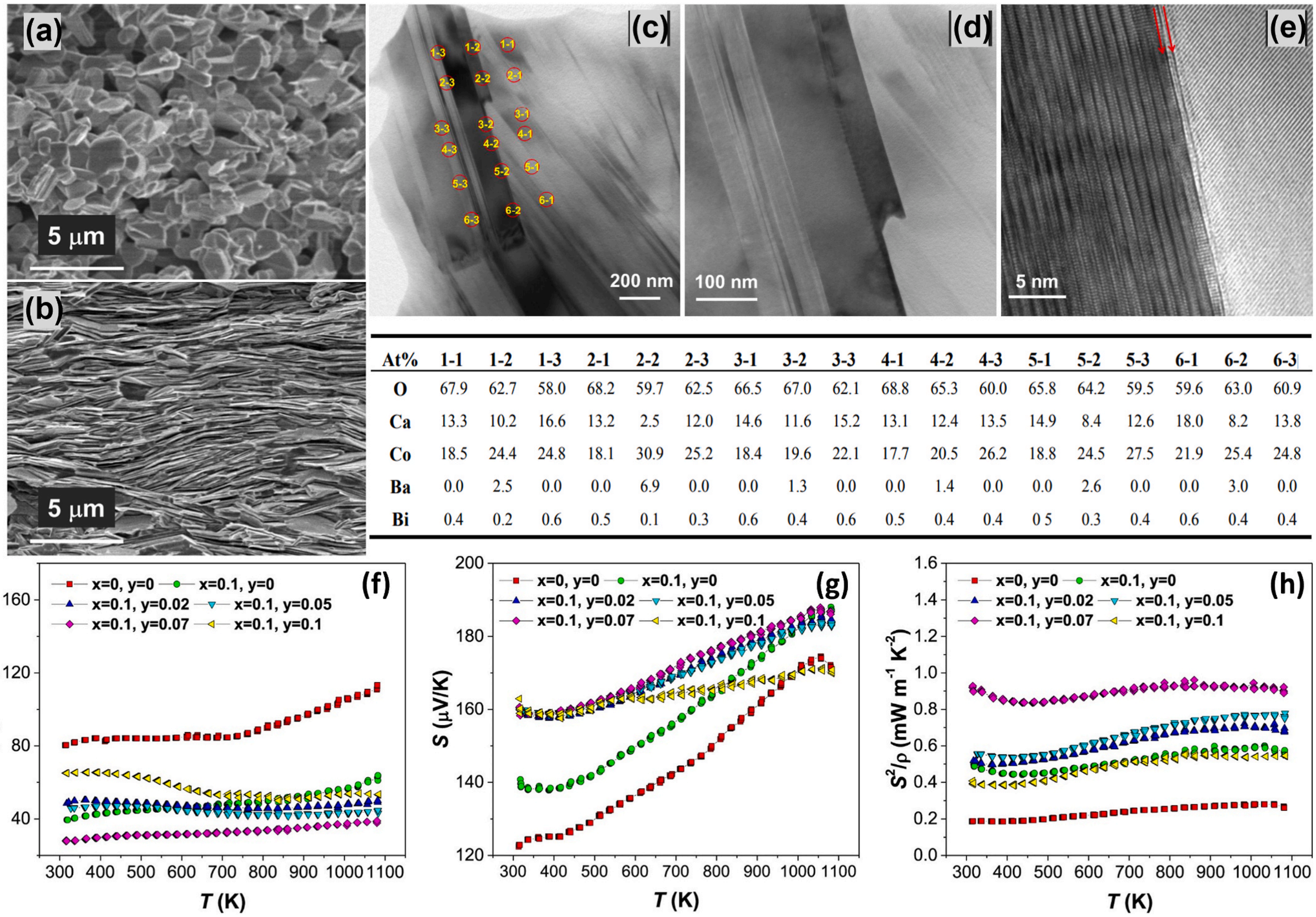

At%	1-1	1-2	1-3	2-1	2-2	2-3	3-1	3-2	3-3	4-1	4-2	4-3	5-1	5-2	5-3	6-1	6-2	6-3
O	67.9	62.7	58.0	68.2	59.7	62.5	66.5	67.0	62.1	68.8	65.3	60.0	65.8	64.2	59.5	59.6	63.0	60.9
Ca	13.3	10.2	16.6	13.2	2.5	12.0	14.6	11.6	15.2	13.1	12.4	13.5	14.9	8.4	12.6	18.0	8.2	13.8
Co	18.5	24.4	24.8	18.1	30.9	25.2	18.4	19.6	22.1	17.7	20.5	26.2	18.8	24.5	27.5	21.9	25.4	24.8
Ba	0.0	2.5	0.0	0.0	6.9	0.0	0.0	1.3	0.0	0.0	1.4	0.0	0.0	2.6	0.0	0.0	3.0	0.0
Bi	0.4	0.2	0.6	0.5	0.1	0.3	0.6	0.4	0.6	0.5	0.4	0.4	0 5	0.3	0.4	0.6	0.4	0.4

Fig. 6. SEM images displaying crystal texture development of (a)$Ca_3Co_4O_{9+\delta}$ and (b)$Ca_{2.9}Bi_{0.1}Ba_{0.07}Co_4O_{9+\delta}$. TEM images (c and d) and HRTEM image (e) from the $Ca_{2.9}Bi_{0.1}Ba_{0.07}Co_4O_{9+\delta}$ sample. The circled numbers show the EDS collected. from two neighboring grains and the surrounding GB area. All the data suggests that GB area is Ba enriched, but Bi depleted which confirms the competing dopant segregation of different sized doping elements. TE properties for the $Ca_{3-x}Bi_xBa_yCo_4O_{9+\delta}$ as function of temperature showing the simultaneously increased S and σ. (a)ρ; (b)S; and (c) $S^2\sigma$. Reprinted from Ceramics International 43 (2017) 11,523–11528, Copyright (2017), with permission from Elsevier.

present the Bi segregation and Tb depletion at the GB plane (Fig. 7). The GBs atomic structure is revealed in greater detail by Z-contrast atomic resolution imaging. In agreement with the TEM EDS results, a brighter column was not observed at the GBs of the $Ca_{2.95}Tb_{0.05}Co_4O_{9+\delta}$ sample (Figs. 7 A-2). This could indicate that Tb is not present at the GBs. Interesting to note, the Bi segregation at the Co sites at the GBs of the $Ca_3Co_4O_{9+\delta}Bi_{0.25}$ sample is indicated by the stronger contrast. In $Ca_{2.95}Tb_{0.05}Co_4O_{9+\delta}Bi_{0.25,}$ on the other hand, along the GB planes, both the Ca and Co sites have highly intense atomic columns. Segregations normally occur with 1–2 atomic spacing onto the Ca sites, whereas the Bi segregation on the Co sites of the rock-salt-type Ca_2CoO_3 misfit layers is considerable (about 3–5 atoms), indicative of the increased Bi segregation due to dual dopants, likely due to Tb depletion at the GB planes [81]. It is worthwhile to mention that the non-stoichiometric addition of Bi is substituting both Ca and Co sites.

In the samples of $Ca_{2.95}Tb_{0.05}Bi_xCo_4O_{9+\delta}$, when Tb is at a fixed level of 0.05, Bi non-stoichiometric addition significantly increased the Seebeck coefficient and decreased the electrical resistivity, as depicted in Fig. 8 (a,b). When the Bi-level is increased to x = 0.25, the sample $Ca_{2.95}Tb_{0.05}Bi_{0.25}Co_4O_{9+\delta}$ exhibits a plateau of high electrical power factor, $S^2\sigma$, of 1.23 $mWm^{-1}K^{-2}$ and 1.83 $mWm^{-1}K^{-2}$ at 1073 and 373 K, respectively, as shown in Fig. 8c. The peak ZT of $Ca_{2.95}Tb_{0.05}Bi_{0.25}Co_4O_{9+\delta}$ is 0.9 at 1073 K, as shown in Fig. 8 (e). The ZT of 0.9 is the greatest ZT value published for $Ca_3Co_4O_{9+\delta}$ ceramics over the previous ten years (Fig. 8f) [29,38,41,45,77,63,82–86]. The sample of $Ca_{2.95}Tb_{0.05}Bi_{0.25}Co_4O_{9+\delta}$ has a high plateau of ZT 0.33 at 373 K and a peak ZT of 0.9 at 1073 K. Such a high plateau leads to the high <u>*average ZT*</u> [87], which is very much desired for high-performance TE materials. The peak ZT of 0.9 is significantly higher than the best reported ZT of 0.61 from $Ca_{2.8}Ag_{0.05}Lu_{0.15}Co_4O_{9+\delta}$ [54] synthesized using SPS. As shown in Fig. 10, the $Ca_{2.95}Tb_{0.05}Bi_xCo_4O_{9+\delta}$ sample surpassed the single-crystal $Ca_3Co_4O_{9+\delta}$ [32] and $Ca_{2.9}Bi_{0.1}Co_4O_{9+\delta}$ single-crystal and exceeded the best reported *p*-type SiGe from 373 K to 973 K [88].

The thermoelectric potential of a material is commonly defined by the ZT value. Nonetheless, the ZT value is comprised of temperature-dependent properties, and, in most cases, this results in the temperature dependence of the ZT value, which in most cases is not linear. Additionally, thermoelectric elements are subject to a significant temperature difference; thus, the ZT_{avg} of the material could provide a better way to understand the overall performance of the materials for TE applications. The average figure of merit is defined as $ZT_{avg}=(1/\Delta T)\int_{Tc}^{Th} Z(T)dT.$ [89] The performance of the average ZT for doped and undoped $Ca_3Co_4O_{9+\delta}$ materials is shown in Fig. 9. The ZT_{avg} of the single crystal $Ca_3Co_4O_{9+\delta}$ reaches a value of 0.37 at 973 K($T_c = 373$ K). Despite the research done in polycrystalline $Ca_3Co_4O_{9+\delta}$ over the last two decades, most reported materials have a ZT_{avg} below 0.24. $Ca_3Co_4O_{9+\delta}Ba_x$ (ZT_{avg} = *0.32*), $Ca_{3-x}Bi_xCo_4O_{9+\delta}$ (ZT_{avg} = *0.29*), Ag (ZT_{avg} = *0.32), and* $Ca_{3-x}Tb_xCo_4O_{9+\delta}Bi_y$ *(*ZT_{avg} = *0.62), and* $Ca_{3x}Tb_xPr_xCo_4O_{9+\delta}Bi_y$*(*$ZT_{avg}$ =

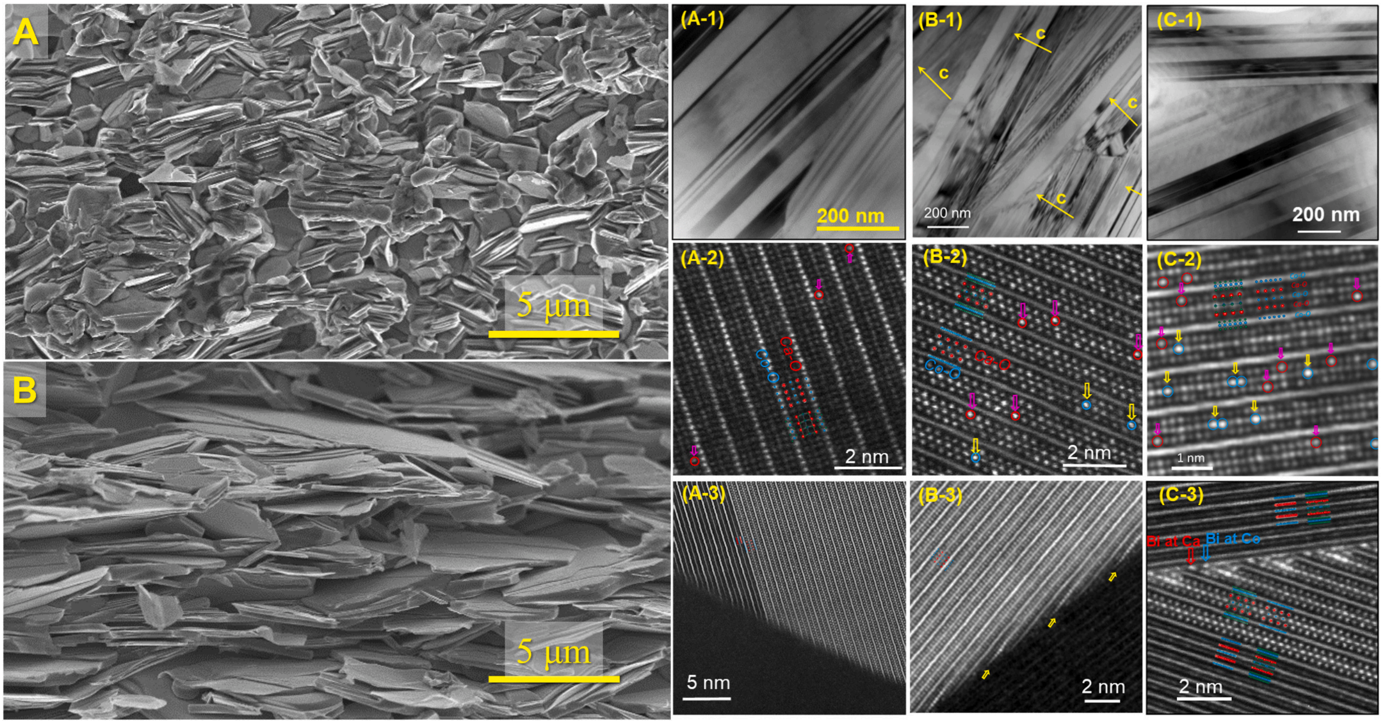

Fig. 7. Cross-sectional SEM images from the fractured surface after sintering stage displaying the improved crystal texture and grain growth for the undoped (A) $Ca_3Co_4O_{9+\delta}$ and dual-doped (B) $Ca_{2.95}Tb_{0.05}Co_4O_{9+\delta}Bi_{0.25}$. TEM and STEM images displaying the nanostructure of the $Ca_{3-x}Tb_xCo_4O_{9+\delta}Bi_y$ samples. (A-), (B-), and (C-) display the lattice nanostructure and GB for $Ca_{2.95}Tb_{0.05}Co_4O_{9+\delta}$, $Ca_3Co_4O_{9+\delta}Bi_{0.25}$, and $Ca_{2.95}Tb_{0.05}Co_4O_{9+\delta}Bi_{0.25}$, respectively. In (A-2), arrows indicate where Tb is located in the lattice of the rock salt layer CaO. In (B-2, B-3) purple arrows indicate where Bi is located in the rock salt layer CaO inside the lattice, while the yellow arrows indicate where Bi is located in the rock salt layer CoO in both the lattice and GB. In (C-2, C-3), purple arrows indicate the location of dopants in the rock salt layer CaO in both the lattice and GB, while the yellow arrows indicate the location of dopants in the rock salt layer CoO in both the lattice and GB. Reprinted (adapted) with permission from {Chem. Mater. 2020, 32, 22, 9730–9739}. Copyright {2020} American Chemical Society.

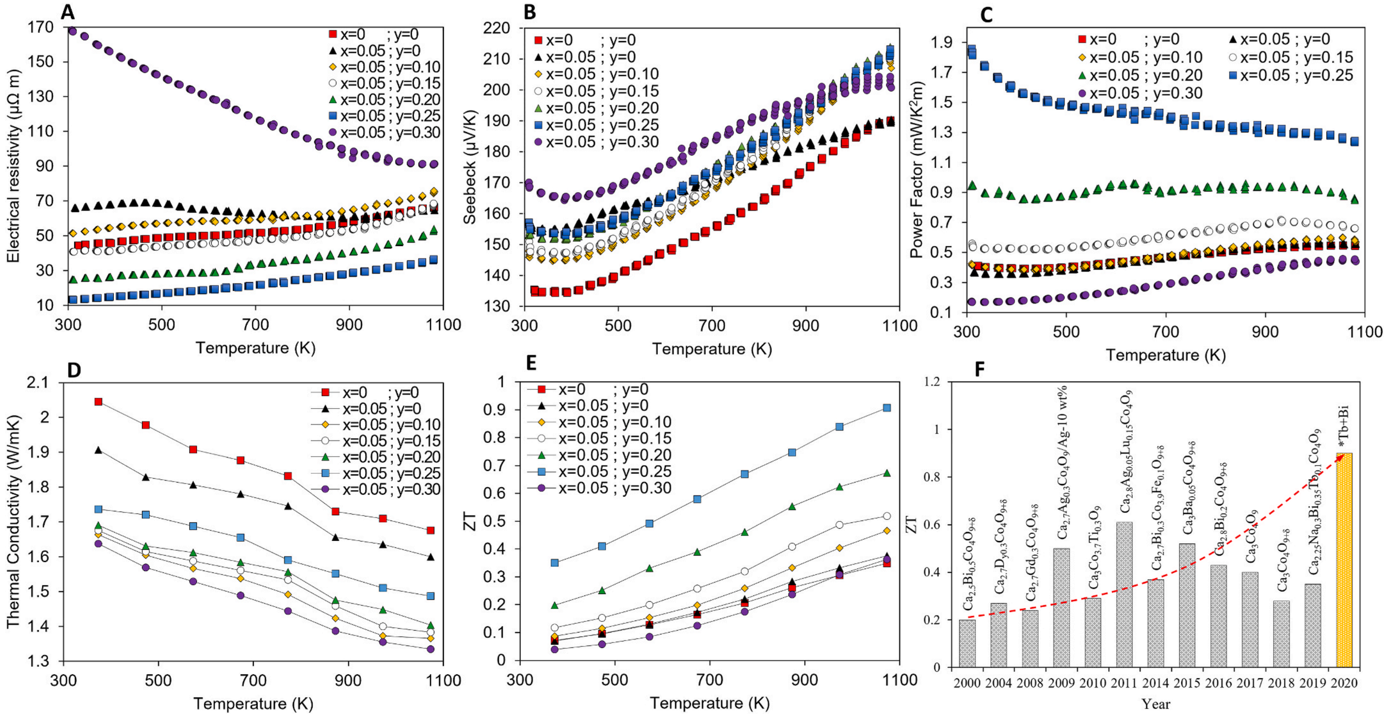

Fig. 8. Temperature dependence of: (A) ρ, (B) S, and (C) $S^2\sigma$ for $Ca_{3-x}Tb_xCo_4O_{9+\delta}Bi_y$; and (D) κ, (E) *ZT* for $Ca_{3-x}Tb_xCo_4O_{9+\delta}Bi_y$ and (F) Timeline of the enhancement in ZT of $Ca_3Co_4O_{9+\delta}$ polycrystalline materials by the inclusion of various doping elements [25,43,56,64–71]. The discussed approach for treating the grain boundaries as a two-dimensional intergranular secondary phase complexion has led to a ZT of 0.9 for the polycrystalline $Ca_3Co_4O_{9+\delta}$. Reprinted (adapted) with permission from {Chem. Mater. 2020, 32, 22, 9730–9739}. Copyright {2020} American Chemical Society.

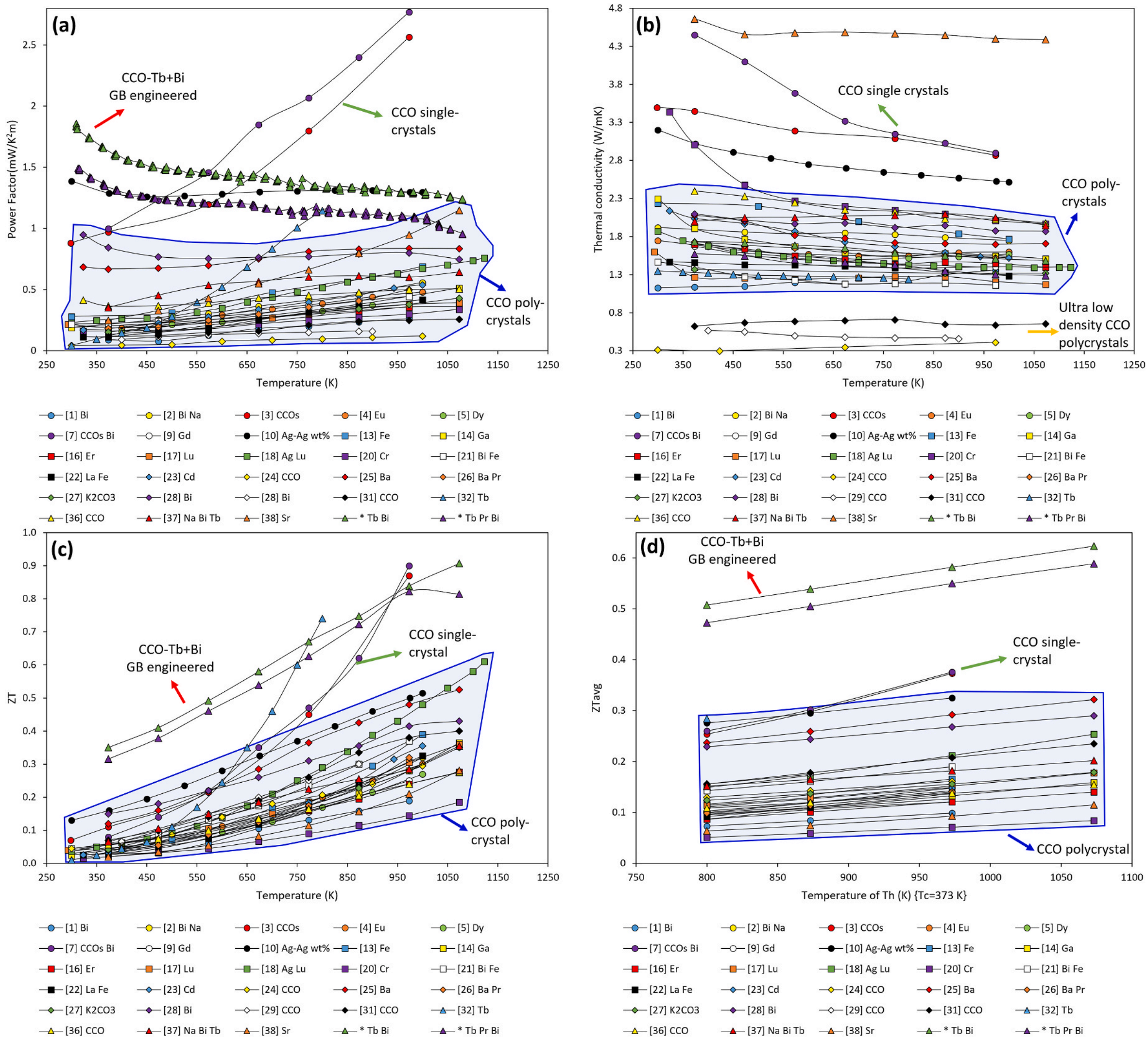

Fig. 9. Temperature dependence of thermoelectric properties of $Ca_3Co_4O_{9+\delta}$ materials. (a) *κ-T*, (b) S^2/ρ*-T,* (c)*ZT-T,* and (d) ZT_{avg}*-T*. The polycristalline $Ca_3Co_4O_{9+\delta}$ materials with engineered GBs outperform the electrical power factor of other reported polycrystal $Ca_3Co_4O_{9+\delta}$ materials while achieving a max value of 0.69 for the ZT_{avg} which is more than double the ZT_{avg} below 0.24 for most $Ca_3Co_4O_{9+\delta}$ including the single crystal counterpart.

0.59) are the only $Ca_3Co_4O_{9+\delta}$ ceramics with a ZT_{avg} above 0.25.

The $Ca_3Co_4Ba_xO_{9+\delta}$ sample with dual dopants with ZT of 0.9, the highest ZT for various oxide at elevated temperatures, outperforms the single crystals in terms of both the peaking *ZT* and the average *ZT* of the $Ca_3Co_4O_{9+\delta}$ single crystals. Furthermore, it outperforms the state-of-the-art SiGe [88], which has a peaking *ZT* of 0.95 and an average *ZT* of 0.551 from T_c 373 K to T_h 1073 K. Most of all, $Ca_3Co_4O_{9+\delta}$ ceramics have just 5–10% of the cost of SiGe [90] and will be performing directly in air.

3. Origin of increased *S* and $S^2\sigma$ and outlook for further performance enhancement

3.1. Driving force and atomic structure origin of dopants GB segregation

In ceramic materials, the driving forces controlling GB segregation can be distinguished as elastic, electrostatic, and dipole interactions [87]. The elastic term arises from interactions between solutes and the ceramic interface due to the space charge and the tendency of the charged solutes to combine with the defects of the opposite charge in ceramics and to form an electrically neutral complexion. Usually, the GBs of the ceramics, such as those from polycrystalline n-type $SrTiO_3$ [32] have higher resistance than those of the grain interior. The origin of the higher resistance is usually attributed to the excess charge near GBs. Both the experimental results and molecular dynamics simulations revealed a negative GB potential related to the depletion of oxygen vacancy concentrations near the GBs.

The GB with too much segregation of a positive or negative charge might draw point defects of opposite charges from the nearby bulk materials, building up the charges. The Coulomb interactions could be the driving force for segregations at the grain boundaries. The segregation of cations including K^+, Ba^{2+}, Bi^{3+} seems to indicate the $Ca_3Co_4Ba_xO_{9+\delta}$ grain boundary plane of the pristine sample may also be negatively charged with the excess of oxygen ions. Nevertheless, this Coulomb interaction could not explain the depletion of Tb^{3+} at the GB plane. It could not explain the competing dopants segregation between Bi^{3+} and Ba^{2+} at the GBs, for which Ba^{2+} expelled Bi^{3+}. However, it indicates that the $Ca_3Co_4Ba_xO_{9+\delta}$ grain boundaries offer extra sites to accommodate large dopants. Furthermore, the magnitude of the positive charge or the valence state on the type of segregation becomes negligible. Hence, the ionic size effect instead of the Coulomb interaction is proposed as the driving mechanism for the dopant grain GB.

3.2. Crystal texture development and increase of carrier mobility with GB engineering

As aforementioned, to make the oxide ceramics viable for large-scale

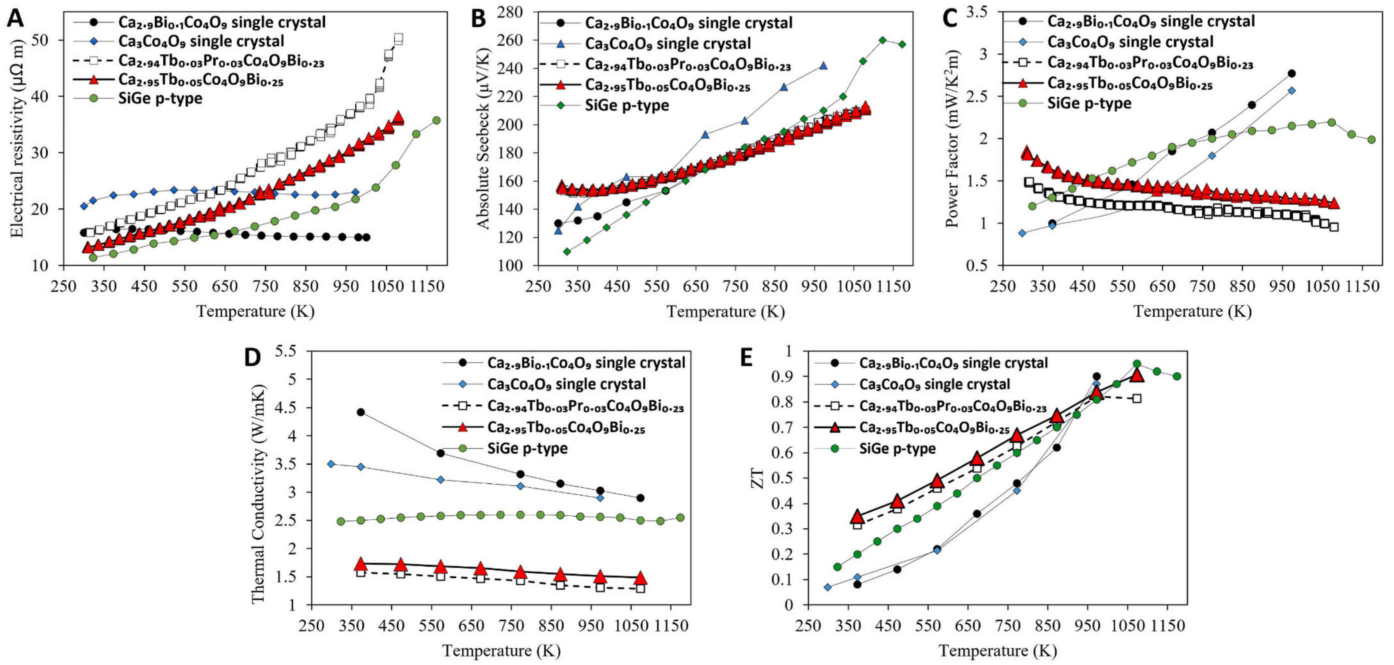

Fig. 10. Thermoelectric properties as function of temperature for several *p*-type materials [23,32,54]: (A) *ρ*, (B) *S,* (C) $S^2\sigma$, (D) κ, and (E) *ZT*. The current approach on grain boundary engineering successfully outperformed the ZT of single crystal $Ca_3Co_4O_{9+\delta}$ and the conventional TE material SiGe. Reprinted (adapted) with permission from {Chem. Mater. 2020, 32, 22, 9730–9739}. Copyright {2020} American Chemical Society.

application, it is mandatory to develop ceramics processing that promotes crystal texture formation using typical cold-pressing and subsequent sintering. During sintering, the GB diffusion is the movement of atoms along the GBs under a driving force, which is mainly the difference in chemical potentials. The doping concentrations control the defect levels, and the diffusion kinetics is susceptible to these values. The present study on $Ca_3Co_4Ba_xO_{9+\delta}$ with oversized dopants indicates that the energetics and diffusion kinetics of the system are strongly affected by dopant segregation, to such an extent that it should control the crystal texture formation. The universal role of over-sized dopant segregation appears to be irrelevant to the valence state. Meanwhile, when two kinds of dopants are present, only one type of dopant seems to be segregating to the GBs. Nevertheless, the exact magnitude of dopants segregation and the concentrations of dopants at the GBs, and the optimum level of dopants segregation that promotes the formation of the crystal texture differ from their bulk values, based on the sign and magnitude of their charge. For the stoichiometric substitution, the optimum Bi doping level is $Ca_{2.75}Bi_{0.25}Co_4O_{9+\delta}$, and for $Ca_3Co_4O_{9+\delta}$ Bi-addition and Tb substitution, the optimum doping is about 0.25.

The effect of K, Ba, and Bi non-stoichiometry addition on the grain growth and texture development of $Ca_3Co_4O_{9+\delta}$ ceramics may be similar to that of SiC and dielectric materials densification using different sintering additives [91]. However, the conventional structural ceramics sintering additives are introduced mainly to achieve a high bulk density, and secondary phase or insulating amorphous phase are often present at the GBs [92]. By contrast, for electroceramics, $Ca_3Co_4O_{9+\delta}$ dopants segregation drastically persists at the GB plane without creating the amorphous or crystal secondary phase, preventing excessive carrier dispersion and a increase in electrical resistivity.

The five sets of samples consistently indicate that the GBs of the $Ca_3Co_4O_{9+\delta}$ ceramics attract large cations. The current findings about the segregation of the large dopant to the GB of calcium cobaltite are somewhat in accordance with those discovered during research on other ceramics like alumina. But between calcium cobaltite and alumina, the effect of the large dopant on the GB diffusion differs. For instance, in alumina, the large dopants significantly slow down the cation diffusion in the GB regime and result in slowing grain growth.

For $Ca_3Co_4O_{9+\delta}$, Bi or K segregation at GBs has triggered the grain growth, while Ba segregation at GB keeps the grain with a similar dimension of that from pristine $Ca_3Co_4O_{9+\delta}$. For all of those samples with GB segregation of dopants, at the optimized level, the segregation of the large dopants reduces the GB energy and speeds up diffusion along the GBs, reducing the GB migration and the crystal texture development, as schematized in Fig. 11. In other words, segregation also serves as the driving force of the establishment and stabilization of crystal texture.

The literature [93,94] showing that dopants GB segregation lowers the GB energy in ceramics is congruent with this aspect of the conclusion about the impact of dopants GB segregation on the crystal texture development. The frequency of GBs during microstructure development has a significant inverse relation with their relative energies. To put it another way, the higher-energy GBs are more certainly to be contracting and lower-energy GBs to be expanding, causing a steady-state distribution of GBs. For this situation, it is the formation of a strong texture along the *c*-axis of monoclinic $Ca_3Co_4O_{9+\delta}$.

3.3. Characteristic temperature dependence of S increase induced by dopants segregation

The improvement in the crystal texture undoubtedly decreases the electrical resistivity by increasing the carrier mobility. Most impressively, once the dopants are segregated at the GBs alone, there is a large increase in the Seebeck coefficient in the low-temperature regime due to the carrier filtering effect. For the five sets of the samples presented in this review, the temperature dependence of the Seebeck coefficient changes depends on the spatial distribution of the dopants. For the $Ca_3Co_4Ba_xO_{9+\delta}$ samples doped with K and Ba, the Seebeck coefficient increase is most pronounced in the low-temperature regime. The increase of the Seebeck coefficient induced by GB dopants segregation gradually decreases with the increase of the measurement temperature and completely diminishes at the high temperature of 1073 K, for which the doped sample has the same Seebeck coefficient as that of the baseline sample. The above results are consistent with the general feature of the GBs on the transport properties. It is commonly accepted that the transport properties at lower temperatures have the greatest impact by

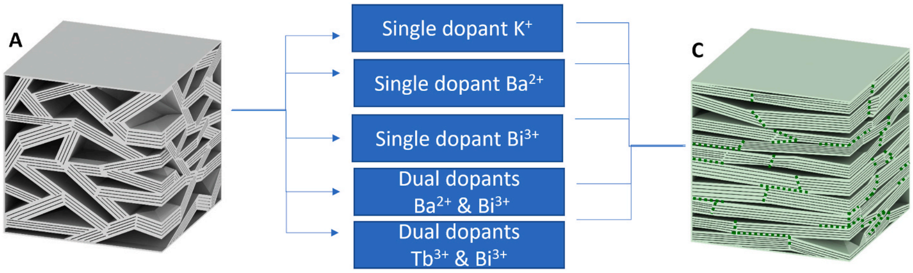

Fig. 11. Schematic showing the undoped (A) $Ca_3Co_4O_{9+\delta}$ and (B) the single and dual element dopant approach to systematically tune the grain boundary and achieve the microstructure evolution. The improved alignment and crystal texture development is achieved with a variety of single and dual elements dopants. Reprinted (adapted) with permission from {Chem. Mater. 2020, 32, 22, 9730–9739}. Copyright {2020} American Chemical Society.

GBs since the weighted mobility degrades by a lesser percentage at high temperatures [53].

The increase of the Seebeck coefficient at both low and high temperatures was achieved for the samples with $Bi^{3+,}$ which demonstrated the Seebeck coefficient was increased due to the intragranular dopants substitution. Competing mechanisms cause the segregation of Ba and the depletion of Bi at the GBs when Bi and Ba are introduced as dopants concurrently, leaving Bi alone in the grain interior. Whereas segregation of Ba at the GBs greatly improves the S at the low-temperature regime, Bi substitution in the lattice enhances the S at both the low and high-temperature regimes. In comparison with the baseline and the sample with the single dopants, the total Seebeck coefficient of the sample with dual dopants is approximately a weighted sum of the increase of the Seebeck coefficient induced by a single dopant.

3.4. *Treating GBs with dopant segregation as the two-dimensional secondary phase complexion with colossal S*

When various nanostructures were introduced to the TE materials systems in 1990, the creation of interfaces, GBs, and nano-inclusions through nanostructuring is one of the most promising approaches. Nevertheless, the GBs can limit the electronic performance of some thermoelectric materials, such as Mg_3Sb_2 and $SrTiO_3$ [95,96]. By stark contrast, in the present case, due to the improvement of the crystal texture, the electrical resistivity was significantly decreased due to the dopant's segregation at the GB. Most strikingly, it is the increase of the Seebeck coefficient constantly and consistently presented in the samples with dopants segregated at the GBs. The increase of the Seebeck coefficient of bulk polycrystalline samples induced by dopants segregation has never been reported before for the TE materials with different chemistry, and the atomic structure source of the increased Seebeck coefficient is worth for a closer look.

The thickness of the segregated layer at the GB is small at ≈ 1–2 nm, and the segregation is extended along the GB plane. The GB segregation is not a complete continuous conformal coverage layer even for the high angle GBs of 45° and low angle GBs of 6° (as shown in Fig. 12). Neither the distribution of the segregation at the nanoscale nor the atomic structure of the segregation region is random. There is an intact channel in between the segregation sites. As such, the GBs can be treated as the secondary phase complexion that is periodically alternating with the segregation region and the non-segregation region. It is an analog to nano-inclusions. The complication is the segregation magnitude varies depending on the misorientation angle of the GBs. For each type of GB with a fixed orientation, the segregation is in regular arrays of constant dimension and spacing.

For each of the single GBs, in this particular case, the segregation nano regions are similar to the nano-inclusions that could serve as the additional scattering centers to scatter the low energy electrons that contribute negatively to the electrons, as schematized in Fig. 12. Low-energy electrons are predominantly scattered in the GB segregation zone, reducing their impact on transport properties and boosting the Seebeck coefficient. Due to the different chemistry and different scattering mechanisms possessed, the GBs associated with dopants segregation can be practically treated as two-dimensional secondary phases that contribute differently to the transport properties than that of the grain interior.

For the samples with different dopants segregating to the GBs, once the GB is treated as the secondary phase, the Seebeck coefficient from the GB phase can be approximated based on the experimental results presented in this review. In the series circuit model, the Seebeck coefficient from the grain and GB complexion are additive. For the baseline samples, the GBs and the grain interiors possess the same Seebeck coefficients, so the baseline Seebeck coefficient can be treated as those of the Seebeck coefficient from the grain interior of the Ba or K doped samples. For the samples with Ba and K dopants that are segregated to the GB alone, the total Seebeck coefficient is a weighted sum of the individual Seebeck coefficients of the grain and GB regions [55] $\alpha = (1 - t_{GB})\alpha_G + t_{GB}{*}\alpha_{GB}$, where t_{GB} is the size fraction (t of GB divided by t of

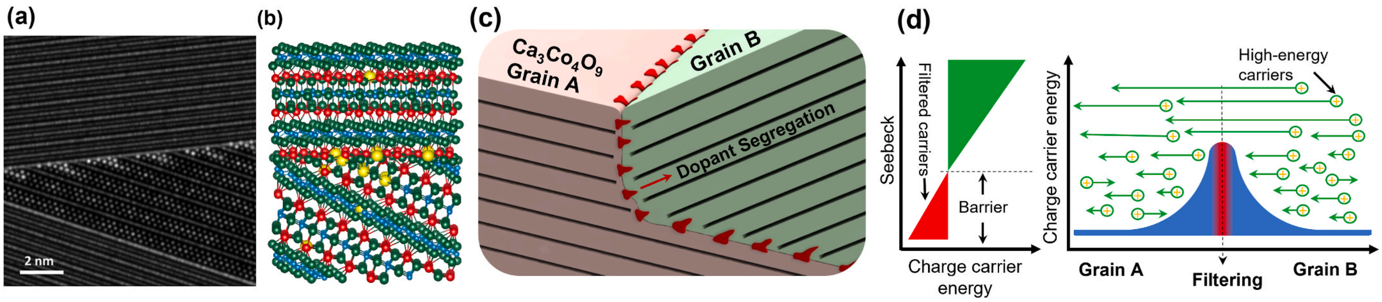

Fig. 12. STEM images displaying the nanostructure of the $Ca_{2.95}Tb_{0.05}Co_4O_{9+\delta}Bi_{0.25}$ for the simulated (a) findings and the 3D crystal structure (b), respectively. (a) and (b) shows the dopant segregation at the grain boundary of grains with different orientation. Reprinted (adapted) with permission from {Chem. Mater. 2020, 32, 22, 9730–9739}. Copyright {2020} American Chemical Society. (c) Schematic representation of grain boundary segregation between two adjacent grains with different crystal orientation. (d) Representation of low energy carrier filtering and their effect in the absolute Seebeck coefficient values. Grain boundary filters low charge carrier that negatively contribute to overall S values, thus, improving the maximum S in the material.

grain) of the grain boundary phase [95]. The GB thickness is estimated to be 1 nm for both samples, and the average grain thickness is 955 nm and 705 nm for the sample of $Ca_3Co_4O_{9+\delta}K_{0.1}$ and $Ca_3Co_4O_{9+\delta}Ba_{0.05}$, respectively. Thus, if we know the total Seebeck ($Ca_3Co_4O_{9+\delta}K_{0.1}$ and $Ca_3Co_4O_{9+\delta}Ba_{0.05}$), the grain Seebeck ($Ca_3Co_4O_{9+\delta}$ baseline), size fraction of t_{GB}, and want to calculate Seebeck of GB, this can be calculated using the equation $\alpha = (1 - t_{GB})\alpha_G + t_{GB}{*}\alpha_{GB}$. The Seebeck coefficient for the samples with K and Ba were calculated in and reported in Fig. 13.

It is noticed that the Seebeck coefficient from the GBs with Ba segregation is higher than that of the GB with K segregation, especially at a higher temperature regime. This difference could be attributed to the larger magnitude of the scattering from Ba, which has a bigger mass than that of K. At room temperature, the Seebeck coefficient for the GBs was calculated as 22,508 μV/K and 29,051 μV/K; this is over 200× of that from the grain interior.

It is worthwhile to point out that, due to the large ionic radius difference, the dopants-segregation region is subjected to a strained interface. The interface strain is also contributing to a big portion of the increased Seebeck coefficient. The entire systems with grain and GBs are thermodynamic equilibrium systems under the conditions that the samples are processed. Due to the large contribution of the strain energy to the interface energy, a separated phase with the exact chemistry dopants segregation regions is unlikely to be in thermodynamic equilibrium or stable. Even though the isolation of the GB phase with a large Seebeck coefficient may not be experimentally feasible, the large Seebeck coefficient from the GB phase indicates a feasible and very appealing approach for dramatically increasing the Seebeck coefficient of bulk ceramics samples through engineering the GBs that are abundant and usually regarded as detrimental to the electrical transport properties. Both the interface strain and the scattering from the segregated oversized atoms are considered as the source of the increase of the Seebeck coefficient through the aforementioned energy filtering effect.

Energy filtering has been investigated theoretically [97,98] and experimentally in an InGaAs/InGaAlAs superlattice that showed an increase in power factor $S^2\sigma$ due to energy filtering effects [99]. Improvement in the Seebeck coefficient due to energy filtering in bulk nanostructured PbTe-based materials have also been reported, however the mobility was negatively impacted and the electrical resistivity was increased [100,101]. In the case of the PbTe with Pb precipitates, the Seebeck coefficient of samples with any given carrier concentration is increased in the sample that contains nano-meter-sized inclusions compared to that of the homogeneous sample [100].

Nevertheless, to our best knowledge, for bulk ceramics, our present work is the first one demonstrating the significant increase of the Seebeck coefficient through GB engineering. Furthermore, different from the nano-precipitates filtering effect that is usually accompanied by decreased carrier mobility and the increased electrical resistivity, this GB filtering effect and its potential impact on the Seebeck coefficient and electrical power factor were not ambiguously observed in other bulk materials systems prior to our study on the $Ca_3Co_4Ba_xO_{9+\delta}$ oxide. When the GBs are treated as a two-dimensional complexion with discrete periodic clusters, it also makes the previous study on the energy filtering effects from two-dimensional materials become relevant to the three-dimensional bulk ceramics.

While the above research will have a direct impact on the development of various TE oxide ceramics, especially those with large anisotropy and require the formation of the crystal texture to ensure high electrical conductivity [102,103], the fundamental knowledge of the GB and interface engineering of ceramic materials, gained from the present research, will be instrumental to many other structural and functional ceramic systems. Those ceramic materials include the superconductors [104–106], ionic conductors [107–111], and the protonic oxide conductors that have transport properties profoundly dominated by the characteristics of the GBs.

3.5. *Promise and challenges for further reduction of κ through nano-inclusions*

It is worthwhile to point out that, when compared to pure $Ca_3Co_4O_{9+\delta}$, which has a peak *ZT* of ≈0.3, $Ca_{2.95}Tb_{0.05}Bi_{0.25}Co_4O_{9+\delta}$ peak ZT of 0.9 is enhanced by ~ 320%, that is mostly accomplished by improving the electrical power factor (Fig. 8c), with only a ≈10% drop in thermal conductivity, as shown in Fig. 8 (d). The lack of the decrease of the thermal conductivity is attributed to the increased density of the samples, increased alignment, especially along the direction that thermal conductivity is measured (orientation dependence of the thermal conductivity in $Ca_3Co_4Ba_xO_{9+\delta}$), and reduced among the high angle GBs.

By tuning the GB intergranular chemistry and grain interior dopant substitution, we successfully decoupled the Seebeck coefficient from the electrical conductivity and significantly improved the power factor by a factor over ≈4.6 at 310 K and ≈2.3 at 1073 K. In the meantime, the high *ZT* from $Ca_{2.95}Tb_{0.05}Bi_{0.25}Co_4O_{9+\delta}$ is attained by using only two dopants to control the GBs. There are no additional defects, such as nano-inclusions introduced to reduce the thermal conductivity. This is considerably different from the approaches utilized for increasing the *ZT* of traditional semiconductors. To present, rather than an enhancement in power factors, the reported substantial *ZT* improvements in a variety of bulk nanostructured materials have been caused by very large decreases in lattice thermal conductivity [112]. The addition of nano-inclusions into bulk-scale TE materials, such as SiGe, Bi_2Te_3, and Si [113] systems, has proved to enhance phonon scattering and reduce thermal conductivity. For $Ca_3Co_4O_{9+\delta}$, the possible route to reduce the thermal conductivity by nano-inclusions has not been explored. This is largely due to the fact that very few elements were identified to be able to form nano-inclusions without reacting with Ca or Co or substituting Ca or Co in the lattice as dopants. The density of the nano-inclusions should be controlled for scattering the phonons while not lowering the

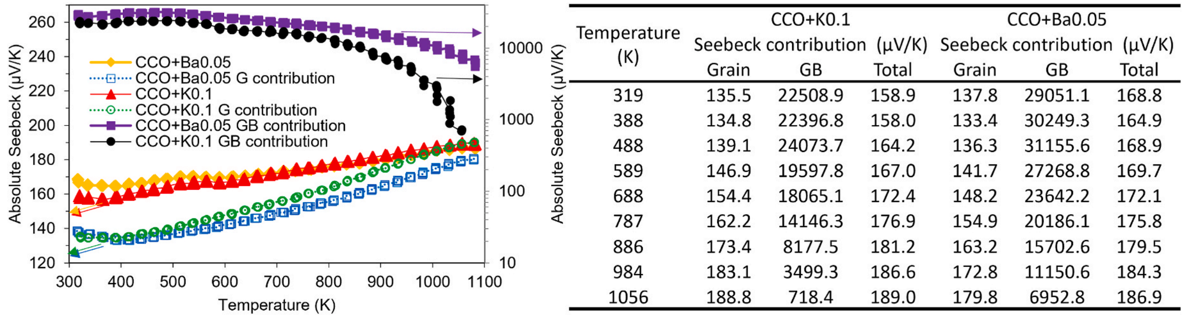

Temperature (K)	CCO+K0.1 Seebeck contribution (μV/K) Grain	GB	Total	CCO+Ba0.05 Seebeck contribution (μV/K) Grain	GB	Total
319	135.5	22508.9	158.9	137.8	29051.1	168.8
388	134.8	22396.8	158.0	133.4	30249.3	164.9
488	139.1	24073.7	164.2	136.3	31155.6	168.9
589	146.9	19597.8	167.0	141.7	27268.8	169.7
688	154.4	18065.1	172.4	148.2	23642.2	172.1
787	162.2	14146.3	176.9	154.9	20186.1	175.8
886	173.4	8177.5	181.2	163.2	15702.6	179.5
984	183.1	3499.3	186.6	172.8	11150.6	184.3
1056	188.8	718.4	189.0	179.8	6952.8	186.9

Fig. 13. Temperature dependence for the grain (G) and the grain boundary (GB) contribution of the overall Seebeck coefficient values of the doped $Ca_3Co_4O_{9+\delta}$. Table on the right shows the numerical values for both the G and GB contribution to the total value of Seebeck for polycrystalline $Ca_3Co_4O_{9+\delta}Ba_{0.05}$ and $Ca_3Co_4O_{9+\delta}K_{0.1}$ samples. The Seebeck coefficient for the GBs was calculated with a value 200 times of that from the grain interior.

electron mobility. A simultaneous increase in the electrical power factor and decrease in the thermal conductivity for the transport in the same directions become possible. For different TE materials, nano-inclusions and nanocomposites could enable the enhancement of the power factor through a modification of the electronic structure or by a carrier filtering effect [19].

3.6. Future perspective of high throughput combinatorial approach & computational design

While the 'grain boundary design' methodology, which involves the incorporation of GB dopants to improve the thermoelectric performance, is effective and innovative, there is an optimum doping level needed for each set of dopants. The discovery of suitable dopant species and the optimum doping level for different TE materials could be accelerated by the high throughput combinatorial approach. The combinatorial synthesis approach [114–117] is an efficient high-throughput technique for the systematic investigation of the compositions and physical properties of a complex system using various screening techniques. Simply stated, combinatorial or high-throughput materials screening is a method that combines the ability for large-scale parallel production of a variety of materials with various high-throughput measurement techniques for a variety of intrinsic and performance properties. This technique was first developed to study drug chemistry, where one synthesizes a large number of compounds in parallel, followed by screening [118].

To study thermoelectric materials, the combinatorial synthesis approach generally entails generating libraries on a substrate with compositions that vary across numerous members using physical vapor deposition techniques, then evaluating the film libraries using high-throughput property screening instruments [18,119,120]. From the screening results of the film libraries, one can obtain a preliminary estimate of the composition regions with highly desirable properties (commonly called the 'sweet spots'). One will have an opportunity to study in detail the refined compositions by preparing bulk materials based on the screened results. Using this high throughput scheme in conjunction with the grain boundary approach, a much more efficient strategy could be designed.

Taking NIST's high throughput approach as an example, the combinatorial thin-film synthesis systems include a PLD component for synthesizing oxide films with a composition-spread method, and a sputtering component for preparing intermetallic films [18,119,120]. For the sputtering component, the thin film deposition approach will use a three-target (A, B, and C) sputter deposition system with a movable shutter over a substrate to deposit overlapping layers of each target. The thickness and shape of the film are controlled by the motion of the shutter. The result will be a graded three-end-member composition. This process is computer-controlled and can be cycled many times for desired film thickness. Thin-film samples may either be deposited on heated substrates or annealed post-deposition to assure compositional uniformity through the film thickness and to promote film crystallization.

The efficiency of the thermoelectric material is measured by power factor; the NIST screening tool system consists of a room-temperature and a high-temperature power factor screening tool [18,119,120], and a thermal effusivity screening tool. In addition to measuring films, these tools can also be used to measure bulk samples with flat surfaces. Measurements are fully automated. This system was later modified so it could rapidly determine the Seebeck coefficient and sheet resistance for thermoelectric films from room-temperature to ≈800 K with high spatial resolution. The details of this instrumentation for measuring the Seebeck coefficient, developed at NIST, have been described in Ref. [121]. To test the thermoreflectance of a combinatorial film, a scanning thermal effusivity measuring device utilizing the frequency domain thermoreflectance approach under periodic heating was designed [122]. Examples of the application using these techniques on thermoelectric materials, such as composition-spread films, conventional thin films, bulk ceramics, ribbons/tapes, and single crystals have been reported [123].

Overall, in the present study, the secondary phase complexion possesses a magnitudes higher Seebeck coefficient than that of the intragrain, as elucidated in Figs. 12 and 13. Such discoveries are undoubtedly consistent with the design principle of high-performance thermoelectric materials in the thin film or bulk-scale composite [17,124]. Uniquely demonstrated in the present study is the realization of designing the grain boundaries, rather than interfaces, on the thermoelectric oxide that is at the very cusp for large-scale waste high-temperature heat recovery and thermal management and leading us to enter the new era for the thermometric oxide ceramics. The high throughput combinatorial approach could be further coupled with high-throughput computation [125] for facilitating and accelerating materials design with ZT magnitudes higher than the state-of-the-art.

4. Conclusion remarks

Understanding the engineering approaches to tune the performance of various TE materials has stimulated intense theoretical and experimental work during the past decades. The major effort is to increase the GB density and increases the scattering of phonons to lower the thermal conductivity. Nevertheless, the GB structure for various TE materials is poorly understood, and the approaches for improving TE performance by enhancing the electrical transport properties, especially the Seebeck coefficient, are completely lacking. The present work leads to the identification of the key nanostructure engineering processes necessary to improve the Seebeck coefficient through GB engineering and the dopant's segregation. The five sets of dopants consistently demonstrate that the oversized dopants segregate to the GBs and subsequently result in the formation of the crystal texture, the increase of the carrier mobility, and the increased Seebeck coefficient due to the carrier filtering effect. It was experimentally validated that through engineering the GBs, such as using dopants segregating to the GBs, the bulk ceramics could have increased carrier mobility while enhancing the Seebeck coefficient and have a net increase in power factor of up to a factor of ≈4.6 at 310 K and ≈2.3 at 1073 K. Furthermore, it reveals the atomic structure origin of the dopant's segregation, and oversized dopants are the driving force while columbic interactions are negligible. Due to the distinct atomic structure of GBs, the GBs should be treated as the complexions that is associated with the discrete channels and strain field. The Seebeck coefficient from such GB complexions is estimated to be over two orders of magnitude from the grain interior over a wide temperature range. When the GBs can be treated as the secondary phase, it can successfully decouple two intrinsic strongly correlated properties between the Seebeck coefficient and electrical conductivity. Even though the isolation of the GB phase with a large Seebeck coefficient may not be experimentally feasible, the large Seebeck coefficient from the GB phase indicates a feasible and very appealing approach for dramatically increasing the Seebeck coefficient of bulk ceramics samples through engineering the GBs that are abundant and usually regarded as detrimental to the electrical transport properties. The present work tuning the TE oxide ceramics through designing the GBs and interfaces will create a platform for the rational design, judicious selection, and effective fabrication of novel ceramics for future electronic and energy applications.

Declaration of competing interest

The authors declare that they have no known competing financial interests or personal relationships that could have appeared to influence the work reported in this paper.

Data availability

Data will be made available on request.

Acknowledgments

We gratefully acknowledge financial support from the National Science Foundation (NSF 1916581).

References

[1] Obara S, Tanaka R. Waste heat recovery system for nuclear power plants using the gas hydrate heat cycle. Appl Energy 2021;292:116667.
[2] Krothapalli A, Greska B. Concentrated solar thermal power. In: Chen WY, Suzuki T, Lackner M, editors. Handbook of climate change mitigation and adaptation. New York: Springer; 2014. p. 1503–36.
[3] Brückner S, Liu S, Miró L, Radspieler M, Cabeza LF, Lävemann E. Industrial waste heat recovery technologies: an economic analysis of heat transformation technologies. Appl Energy 2015;151:157–67.
[4] Ates F, Ozcan H. Turkey's industrial waste heat recovery potential with power and hydrogen conversion technologies: a techno-economic analysis. Int J Hydrogen Energy 2022;47(5):3224–36.
[5] Hendricks T, Choate WT. Engineering scoping study of thermoelectric generator systems for industrial waste heat recovery. Richland, WA: Pacific Northwest National Lab.; 2006.
[6] U.S. Department of Energy. Quadrennial Technology. Review 2015: technology assessments - innovating clean energy technologies in advanced manufacturing. United States; 2015.
[7] DiSalvo FJ. Thermoelectric cooling and power generation. Science 1999;285(5428):703–6.
[8] Bell LE. Cooling, heating, generating power, and recovering waste heat with thermoelectric systems. Science 2008;321(5895):1457–61.
[9] Tritt TM. Thermoelectric phenomena, materials, and applications. Annu Rev Mater Res 2011;41:433–48.
[10] Taylor PJ, Maddux JR, Wilson A. Evaluation of thermoelectric devices by the slope-efficiency method. Adelphi, MD: US Army Research Laboratory; 2016.
[11] Zebarjadi M, Esfarjani K, Dresselhaus M, Ren Z, Chen G. Perspectives on thermoelectrics: from fundamentals to device applications. Energy Environ Sci 2012;5(1):5147–62.
[12] Snyder GJ, Toberer ES. Complex thermoelectric materials. In: Materials for sustainable energy: a collection of peer-reviewed research and review articles from Nature Publishing Group. World Scientific Publishing Co.; 2010. p. 101–10.
[13] He J, Tritt TM. Advances in thermoelectric materials research: looking back and moving forward. Science 2017;357(6358):eaak9997.
[14] Mun H, Choi SM, Lee KH, Kim SW. Boundary engineering for the thermoelectric performance of bulk alloys based on bismuth telluride. ChemSusChem 2015;8(14):2312–26.
[15] Rowe DM. Thermoelectrics handbook: macro to nano. Boca Raton: CRC Press; 2006.
[16] Kirkham MJ, dos Santos AM, Rawn CJ, Lara-Curzio E, Sharp JW, Thompson AJ. Abinitio determination of crystal structures of the thermoelectric material MgAgSb. Phys Rev B 2012;85(14):144120.
[17] Hinterleitner B, Knapp I, Poneder M, Shi Y, Müller H, Eguchi G, et al. Thermoelectric performance of a metastable thin-film Heusler alloy. Nature 2019;576:85–90.
[18] Otani M, Lowhorn N, Schenck PK, Wong-Ng W, Green ML, Itaka K, et al. A high-throughput thermoelectric power-factor screening tool for rapid construction of thermoelectric property diagrams. Appl Phys Lett 2007;91(13):132102.
[19] Borup KA, De Boor J, Wang H, Drymiotis F, Gascoin F, Shi X, et al. Measuring thermoelectric transport properties of materials. Energy Environ Sci 2015;8(2):423–35.
[20] Paredes-Navia SA, Liang L, Romo-De-La-Cruz CO, Gemmen E, Fernandes A, Prucz J, et al. Electrical conductivity increase by order of magnitude through controlling sintering to tune hierarchical structure of oxide ceramics. J Solid State Chem 2021;294:121831.
[21] Yang J, Yip HL, Jen AKY. Rational design of advanced thermoelectric materials. Adv Energy Mater 2013;3(5):549–65.
[22] Ohta H, Sugiura K, Koumoto K. Recent progress in oxide thermoelectric materials: p-type Ca3Co4O9 and n-type SrTiO3. Inorg Chem 2008;47(19):8429–36.
[23] Hao Q, Xu D, Lu N, Zhao H. High-throughput *ZT* predictions of nanoporous bulk materials as next-generation thermoelectric materials: a material genome approach. Phys Rev B 2016;93(20):205206.
[24] Ma Y, Vartak PB, Nagaraj P, Wang RY. Thermoelectric properties of copper chalcogenide alloys deposited via the solution-phase using a thiol–amine solvent mixture. RSC Adv 2016;6(102):99905–13.
[25] Yan J, Gorai P, Ortiz B, Miller S, Barnett SA, Mason T, et al. Material descriptors for predicting thermoelectric performance. Energy Environ Sci 2015;8(3):983–94.
[26] Alberi K, Nardelli MB, Zakutayev A, Mitas L, Curtarolo S, Jain A, et al. The 2019 materials by design roadmap. J Phys D Appl Phys 2018;52(1):013001.
[27] Xie W, Weidenkaff A, Tang X, Zhang Q, Poon J, Tritt T. Recent advances in nanostructured thermoelectric half-heusler compounds. Nanomaterials 2012;2(4):379–412.
[28] Poudel B, Hao Q, Ma Y, Lan Y, Minnich A, Yu B, et al. High-thermoelectric performance of nanostructured bismuth antimony telluride bulk alloys. Science 2008;320(5876):634–8.
[29] Dresselhaus MS, Chen G, Tang MY, Yang R, Lee H, Wang D, et al. New directions for low-dimensional thermoelectric materials. Adv Mater 2007;19(8):1043–53.
[30] Shuai J, Mao J, Song S, Zhang Q, Chen G, Ren Z. Recent progress and future challenges on thermoelectric Zintl materials. Mater. Today Phys. 2017;1:74–95.
[31] Li S, Funahashi R, Matsubara I, Ueno K, Sodeoka S, Yamada H. Synthesis and thermoelectric properties of the new oxide materials $Ca_{3\text{-}x}Bi_xCo_4O_{9+\delta}$ (0.0< x< 0.75). Chem Mater 2000;12(8):2424–7.
[32] Shikano M, Funahashi R. Electrical and thermal properties of single-crystalline $(Ca_2CoO_3)_{0.7}CoO_2$ with a $Ca_3Co_4O_9$ structure. Appl Phys Lett 2003;82(12):1851–3.
[33] Singh DJ. Quantum critical behavior and possible triplet superconductivity in electron-doped CoO_2 sheets. Phys Rev B 2003;68:020503 [R)].
[34] Terasaki I, Sasago Y, Uchinokura K. Large thermoelectric power in $NaCo_2O_4$ single crystals. Phys Rev B 1997;56(20):12685–7.
[35] Shizuya M, Isobe M, Baba Y, Nagai T, Osada M, Kosuda K, et al. New misfit-layered cobalt oxide (CaOH)(1.14)CoO2. J Solid State Chem 2007;180(1):249–59.
[36] Isobe M, Shizuya M, Takayama-Muromachi E. Crystal structure and physical properties of a misfit-layered cobaltite (CaOH)(1.14)CoO2. J Magn Magn Mater 2007;310(2):E269–71.
[37] Miyazaki Y, Onoda M, Oku T, Kikuchi M, Ishii Y, Ono Y, et al. Modulated structure of the thermoelectric compound Ca2CoO3 (0.62)CoO2. J Phys Soc Jpn 2002;71(2):491–7.
[38] De Vaulx C, Julien MH, Berthier C, Hebert S, Pralong V, Maignan A. Electronic correlations in CoO2, the parent compound of triangular cobaltates. Phys Rev Lett 2007;98(24):246402.
[39] Matsubara I, Funahashi R, Shikano M, Sasaki K, Enomoto H. Cation substituted (Ca2CoO3)(x)CoO2 films and their thermoelectric properties. Appl Phys Lett 2002;80(25):4729–31.
[40] Xu G, Funahashi R, Shikano M, Pu Q, Liu B. High temperature transport properties of Ca3-xNaxCo4O9 system. Solid State Commun 2002;124(3):73–6.
[41] Hu YF, Si WD, Sutter E, Li Q. In situ growth of c-axis-oriented $Ca_3Co_4O_9$ thin films on Si(100). Appl Phys Lett 2005;86(8):082103.
[42] Pravarthana D, Lebedev O, Hebert S, Chateigner D, Salvador P, Prellier W. High-throughput synthesis of thermoelectric $Ca_3Co_4O_9$ films. Appl Phys Lett 2013;103(14):143123.
[43] Butt S, Xu W, He WQ, Tan Q, Ren GK, Lin Y, et al. Enhancement of thermoelectric Performance in Cd-doped $Ca_3Co_4O_9$ via spin entropy, defect chemistry and phonon scattering. J Mater Chem 2014;2(45):19479–87.
[44] Masset AC, Michel C, Maignan A, Hervieu M, Toulemonde O, Studer F, et al. Misfit-layered cobaltite with an anisotropic giant magnetoresistance: $Ca_3Co_4O_9$. Phys Rev B 2000;62(1):166–75.
[45] Koumoto K, Funahashi R, Guilmeau E, Miyazaki Y, Weidenkaff A, Wang YF, et al. Thermoelectric ceramics for energy harvesting. J Am Ceram Soc 2013;96(1):1–23.
[46] Katsuyama S, Takiguchi Y, Ito M. Synthesis of $Ca_3Co_4O_9$ ceramics by polymerized complex and hydrothermal hot-pressing processes and the investigation of its thermoelectric properties. J Mater Sci 2008;43(10):3553–9.
[47] Wang Y, Sui Y, Wang XJ, Su WH. Enhancement of thermoelectric efficiency in (Ca, Dy)MnO(3)-(Ca, Yb)MnO(3) solid solutions. Appl Phys Lett 2010;97(5):052109.
[48] Kenfaui D, Bonnefont G, Chateigner D, Fantozzi G, Gomina M, Noudem JG. $Ca_3Co_4O_9$ ceramics consolidated by SPS process: optimisation of mechanical and thermoelectric properties. Mater Res Bull 2010;45(9):1240–9.
[49] Zhou YQ, Matsubara I, Horii S, Takeuchi T, Funahashi R, Shikano M, et al. Thermoelectric properties of highly grain-aligned and densified Co-based oxide ceramics. J Appl Phys 2003;93(5):2653–8.
[50] Zhang YF, Zhang JX, Lu QM. Synthesis of highly textured $Ca_3Co_4O_9$ ceramics by spark plasma sintering. Ceram Int 2007;33(7):1305–8.
[51] Fergus JW. Oxide materials for high temperature thermoelectric energy conversion. J Eur Ceram Soc 2012;32(3):525–40.
[52] Song X, Chen Y, Chen S, Barbero E, Thomas EL, Barnes P. Significant enhancement of electrical transport properties of thermoelectric Ca3Co4O9+δ through Yb doping. Solid State Commun 2012;152(16):1509–12.
[53] Xiang P-H, Kinemuchi Y, Kaga H, Watari K. Fabrication and thermoelectric properties of Ca3Co4O9/Ag composites. J Alloys Compd 2008;454(1–2):364–9.
[54] Nong NV, Pryds N, Linderoth S, Ohtaki M. Enhancement of the thermoelectric performance of p-type layered oxide $Ca_3Co_4O_{9+\delta}$ through heavy doping and metallic nanoinclusions. Adv Mater 2011;23(21):2484–90.
[55] Dylla MT, Kuo JJ, Witting I, Snyder GJ. Grain boundary engineering nanostructured SrTiO3 for thermoelectric applications. Adv Mater Interfac 2019;6(15):1900222.
[56] Boyle C, Liang L, Romo-De-La-Cruz C-O, Johnson R, Chen Y, Prucz J, et al. Improving the thermoelectric Performance and thermal stability of Ca 3 Co 4 O 9 + δ ceramics by sintering in oxygen atmosphere. J Sol Gel Sci Technol 2018;85(3):712–22.
[57] Bowman WJ, Kelly MN, Rohrer GS, Hernandez CA, Crozier PA. Enhanced ionic conductivity in electroceramics by nanoscale enrichment of grain boundaries with high solute concentration. Nanoscale 2017;9(44):17293–302.
[58] Lee JH, Kim I, Hulbert DM, Jiang D, Mukherjee AK, Zhang X, et al. Grain and grain boundary activities observed in alumina–zirconia–magnesia spinel nanocomposites by in situ nanoindentation using transmission electron microscopy. Acta Mater 2010;58(14):4891–9.
[59] Flewitt PEJ, Wild RK. Grain boundaries: their microstructure and chemistry. John Wiley and Sons, LTD; 2001.
[60] Tschöpe A, Kilassonia S, Zapp B, Birringer R. Grain-size-dependent thermopower of polycrystalline cerium oxide. Solid State Ionics 2002;149(3–4):261–73.

[61] Kim SI, Lee KH, Mun HA, Kim HS, Hwang SW, Roh JW, et al. Dense dislocation arrays embedded in grain boundaries for high-performance bulk thermoelectrics. Science 2015;348(6230):109–14.

[62] Kenfaui D, Gomina M, Noudem J, Chateigner D. Anisotropy of transport properties correlated to grain boundary density and quantified texture in thick oriented $Ca_3Co_4O_9$ ceramics. Materials 2018;11(7):1224.

[63] Wang Y, Sui Y, Cheng J, Wang X, Su W. Comparison of the high temperature thermoelectric properties for Ag-doped and Ag-added Ca3Co4O9. J Alloys Compd 2009;477(1):817–21.

[64] Chen S, Song X, Chen X, Chen Y, Barbero EJ, Thomas EL, et al. Effect of precursor calcination temperature on the microstructure and thermoelectric properties of $Ca_3Co_4O_9$ ceramics. J Sol Gel Sci Technol 2012;64(3):627–36.

[65] Carvillo P, Chen Y, Boyle C, Barnes PN, Song X. Thermoelectric performance enhancement of calcium cobaltite through barium grain boundary segregation. Inorg Chem 2015;54(18):9027–32.

[66] Song X, McIntyre D, Chen X, Barbero EJ, Chen Y. Phase evolution and thermoelectric performance of calcium cobaltite upon high temperature aging. Ceram Int 2015;41(9):11069–74.

[67] Boyle C, Carvillo P, Chen Y, Barbero EJ, Mcintyre D, Song X. Grain boundary segregation and thermoelectric performance enhancement of bismuth doped calcium cobaltite. J Eur Ceram Soc 2016;36(3):601–7.

[68] Boyle C, Liang L, Chen Y, Prucz J, Cakmak E, Watkins TR, et al. Competing dopants grain boundary segregation and resultant seebeck coefficient and power factor enhancement of thermoelectric calcium cobaltite ceramics. Ceram Int 2017;43(14):11523–8.

[69] Talley K, Barron S, Nguyen N, Wong-Ng W, Martin J, Zhang Y, et al. Thermoelectric properties of the $LaCoO_3$-$LaCrO_3$ system using a high-throughput combinatorial approach. Solid State Sci 2017;64:7–12.

[70] Song X, Paredes Navia SA, Liang L, Boyle C, Romo-De-La-Cruz CO, Jackson B, et al. Grain boundary phase segregation for dramatic improvement of the thermoelectric performance of oxide ceramics. ACS Appl Mater Interfaces 2018;10(45):39018–24.

[71] Romo-De-La-Cruz C, Liang L, Navia SAP, Chen Y, Prucz J, Song X. Role of oversized dopant potassium on the nanostructure and thermoelectric performance of calcium cobaltite ceramics. Sustain Energy Fuels 2018;2(4):876–81.

[72] Wu N, Holgate TC, Van Nong N, Pryds N, Linderoth S. High temperature thermoelectric properties of $Ca_3Co_4O_{9+\delta}$ by auto-combustion synthesis and spark plasma sintering. J Eur Ceram Soc 2014;34(4):925–31.

[73] Hu Z, Zhang H, Wang J, Chen L, Xie X, Liu X, et al. Fabrication and thermosensitive characteristics of BaCoO 3− δ ceramics for low temperature negative temperature coefficient thermistor. J Mater Sci Mater Electron 2017;28(8):6239–44.

[74] Mikami M, Chong K, Miyazaki Y, Kajitani T, Inoue T, Sodeoka S, et al. Bi-substitution effects on crystal structure and thermoelectric properties of $Ca_3Co_4O_9$ single crystals. Jpn. J. Appl. Phys. Part 1 - Regul. Pap. Brief Commun. Rev. Pap. 2006;45(5A):4131–6.

[75] Mikami M, Ando N, Guilmeau E, Funahashi R. Effect of Bi substitution on microstructure and thermoelectric properties of polycrystalline Ca_2CoO_3 (p) CoO_2. Jpn. J. Appl. Phys. Part 1 - Regul. Pap. Brief Commun. Rev. Pap. 2006;45(5A):4152–8.

[76] Prevel M, Perez O, Noudem JG. Bulk textured $Ca_{2.5}(RE)_{0.5}Co_4O_9$ (RE: Pr, Nd, Eu, Dy and Yb) thermoelectric oxides by sinter-forging. Solid State Sci 2007;9(3–4):231–5.

[77] Saini S, Yaddanapudi HS, Tian K, Yin Y, Magginetti D, Tiwari A. Terbium ion doping in $Ca_3Co_4O_9$: a step towards high-performance thermoelectric materials. Sci Rep 2017;7:44621.

[78] Bhaskar A, Jhang CS, Liu CJ. Thermoelectric Properties of $Ca_{3-x}Dy_xCo_4O_{9+\delta}$ with x= 0.00, 0.02, 0.05, and 0.10. J Electron Mater 2013;42(8):2582–6.

[79] Zhang F, Zhang X, Lu Q, Zhang J, Liu Y, Zhang G. Effects of Pr doping on thermoelectric transport properties of $Ca_{3-x}Pr_xCo_4O_9$. Solid State Sci 2011;13(7):1443–7.

[80] Noviyanto A, Yoon DH. Rare-earth oxide additives for the sintering of silicon carbide. Diam Relat Mater 2013;38:124–30.

[81] Romo-De-La-Cruz CO, Chen Y, Liang L, Williams M, Song X. Thermoelectric oxide ceramics outperforming single crystals enabled by dopant segregations. Chem Mater 2020;32(22):9730–9.

[82] Wang D, Chen L, Yao Q, Li J. High-temperature thermoelectric properties of $Ca_3Co_4O_9$+δ with Eu substitution. Solid State Commun 2004;129(9):615–8.

[83] Wang Y, Sui Y, Cheng J, Wang X, Su W. The thermal-transport properties of the Ca3−xAgxCo4O9 system (0≤x≤0.3). J Phys Condens Matter 2007;19(35):356216.

[84] Liu HQ, Zhao XB, Liu F, Song Y, Sun Q, Zhu TJ, et al. Effect of Gd-doping on thermoelectric properties of Ca3Co4O9+δ ceramics. J Mater Sci 2008;43(21):6933–7.

[85] Nong NV, Liu CJ, Ohtaki M. Improvement on the high temperature thermoelectric performance of Ga-doped misfit-layered Ca3Co4−xGaxO9+δ (x=0, 0.05, 0.1, and 0.2). J Alloys Compd 2010;491(1):53–6.

[86] Klyndyuk AI, Matsukevich IV. Synthesis and properties of Ca2.8Ln0.2Co4O9+δ (Ln=La, Nd, Sm, Tb-Er) solid solutions. Inorg Mater 2012;48(10):1052–7.

[87] Lejcek P. Grain boundary segregation in metals. Berlin: Springer; 2010.

[88] Joshi G, Lee H, Lan Y, Wang X, Zhu G, Wang D, et al. Enhanced thermoelectric figure-of-merit in nanostructured p-type silicon germanium bulk alloys. Nano Lett 2008;8(12):4670–4.

[89] Kim HS, Liu W, Chen G, Chu C-W, Ren Z. Relationship between thermoelectric figure of merit and energy conversion efficiency. Proc Natl Acad Sci USA 2015;112(27):8205–10.

[90] LeBlanc S, Yee SK, Scullin ML, Dames C, Goodson KE. Material and manufacturing cost considerations for thermoelectrics. Renew Sustain Energy Rev 2014;32:313–27.

[91] Noviyanto A, Yoon DH. Metal oxide additives for the sintering of silicon carbide: reactivity and densification. Curr Appl Phys 2013;13(1):287–92.

[92] Bhuyan R, Kumar TS, Pamu D. Liquid phase effect of Bi2O3 additive on densification, microstructure and microwave dielectric properties of Mg_2TiO_4 ceramics. Ferroelectrics 2017;516(1):173–84.

[93] Rohrer GS. Measuring and interpreting the structure of grain-boundary networks. J Am Ceram Soc 2011;94(3):633–46.

[94] Papillon F, Rohrer GS, Wynblatt P. Effect of segregating impurities on the grain-boundary character distribution of magnesium oxide. J Am Ceram Soc 2009;92(12):3044–51.

[95] Kuo JJ, Kang SD, Imasato K, Tamaki H, Ohno S, Kanno T, et al. Energy Environ Sci 2018;11:429.

[96] Mahmud I, Yoon MS, Kim IH, Choi MK, Ur SC. Thermoelectric properties of the ceramic oxide Sr1−x La x TiO3. J Kor Phys Soc 2016;68:35–40.

[97] Vashaee D, Shakouri A. Improved thermoelectric power factor in metal-based superlattices. Phys Rev Lett 2004;92(10):106103.

[98] Kim W, Zide J, Gossard A, Klenov D, Stemmer S, Shakouri A, et al. Thermal conductivity reduction and thermoelectric figure of merit increase by embedding nanoparticles in crystalline semiconductors. Phys Rev Lett 2006;96(4):045901.

[99] Zide JMO, Vashaee D, Bian ZX, Zeng G, Bowers JE, Shakouri A, et al. Demonstration of electron filtering to increase the Seebeck coefficient in In0.53Ga0.47As/In0.53Ga0.28Al0.19As superlattices. Phys Rev B 2006;74(20):205335.

[100] Heremans JP, Thrush CM, Morelli DT. Thermopower enhancement in PbTe with Pb precipitates. J Appl Phys 2005;98(6):063703.

[101] Heremans JP, Thrush CM, Morelli DT. Thermopower enhancement in lead telluride nanostructures. Phys Rev B 2004;70(11):115334.

[102] Sparks TD, Gurlo A, Gaultois MW, Clarke DR. Revised model for thermopower and site inversion in Co_3O_4 spinel. Phys Rev B 2018;98(2):024108.

[103] Liang X, Bell D, Clarke DR. Single layer in-O atomic sheets as phonon and electron and barriers in ZnO-In_2O_3 natural superlattices: implications for thermoelectricity. J Appl Phys 2018;124(2):025101.

[104] Song X, Daniels G, Feldmann DM, Gurevich A, Larbalestier D. Electromagnetic, atomic structure and chemistry changes induced by Ca-doping of low-angle $YBa_2Cu_3O_{7-\delta}$ grain boundaries. Nat Mater 2005;4(6):470.

[105] Eom C, Lee M, Choi J, Belenky L, Song X, Cooley L, et al. High critical current density and enhanced irreversibility field in superconducting MgB_2 thin films. Nature 2001;411(6837):558.

[106] Song X, Chen Z, Kim S-I, Feldmann DM, Larbalestier D, Reeves J, et al. Evidence for strong flux pinning by small, dense nanoprecipitates in a Sm-doped $YBa_2Cu_3O_{7-\delta}$ coated conductor. Appl Phys Lett 2006;88(21):212508.

[107] Chen Y, Chen S, Hackett G, Finklea H, Song X, Gerdes K. Microstructural and chemical evolution near anode triple phase boundary in Ni/YSZ solid oxide fuel cells. Solid State Ionics 2011;204–205:87–90.

[108] Chen S, Chen Y, Finklea H, Song X, Hacket G, Gerdes K. Crystal defects of yttria stabilized zirconia in Solid Oxide Fuel Cells and their evolution upon cell operation. Solid State Ionics 2012;206:104–11.

[109] Nielsen BC, Gerdes K, O'Connor W, Song X, Abernathy H. Partitioning of coal contaminants in the components of liquid tin anode solid oxide fuel cells. J Power Sources 2012;211:192–201.

[110] Hackett GA, Gerdes K, Song X, Chen Y, Shutthanandan V, Engelhard M, et al. Performance of solid oxide fuel cells operated with coal syngas provided directly from a gasification process. J Power Sources 2012;214:142–52.

[111] Chen Y, Chen S, Hackett G, Finklea H, Zondlo J, Celik I, et al. Microstructure degradation of YSZ in Ni/YSZ anodes of SOFC operated in phosphine-containing fuels. Solid State Ionics 2013;234:25–32.

[112] Kanatzidis MG. Nanostructured thermoelectrics: the new paradigm? Chem Mater 2010;22(3):648–59.

[113] Bhandari CM. Minimizing the thermal conductivity. In: Rowe DM, editor. CRC handbook of thermoelectrics. Boca Raton: CRC; 1995. p. 55–65.

[114] Xiang XD, Takeuchi I. Combinatorial materials synthesis. New York: Marcel Dekker; 2003.

[115] van Dover RB, Schneemeyer LD, Fleming RM. Discovery of a useful thin-film dielectric using a composition-spread approach. Nature 1998;392(6672):162–4.

[116] Yao Y, Huang Z, Li T, Wang H, Liu Y, Stein HS, et al. High-throughput, combinatorial synthesis of multimetallic nanoclusters. Proc Natl Acad Sci USA 2020;117(12):6316–22.

[117] Yang L, Haber JA, Armstrong Z, Yang SJ, Kan K, Zhou L, et al. Discovery of complex oxides via automated experiments and data science. Proc Natl Acad Sci USA 2021;118(37):e2106042118.

[118] Plunkett MJ, Ellman JA. Combinatorial chemistry and new drugs. Sci Am 1977;276(4):68–73.

[119] Otani M, Itaka K, Wong-Ng W, Schenck PK, Koinuma H. Development of high-throughput thermoelectric tool for combinatorial thin film libraries. Appl Surf Sci 2007;254:765–7.

[120] Otani M, Thomas E, Wong-Ng W, Schenck PK, Lowhorn ND, Green ML, et al. A high-throughput screening system for thermoelectric material exploration based on a combinatorial film approach. Jap. J. Appl. Phys 2009;48:05EB02.

[121] Yan YG, Martin J, Wong-Ng W, Green M, Tang XF. A temperature dependent screening tool for high throughput thermoelectric characterization of combinatorial films. Rev Sci Instrum 2013;84:115110.

[122] Wong-Ng W, Yan Y, Martin J, Otani M, Thomas EL, Tang XF, et al. Development and applications of non-destructive screening tools for thermoelectric materials at NIST. Ferroelectrics 2014;470(1):241–59.

[123] Wong-Ng W, Yan Y, Otani M, Martin J, Talley KR, Barron S, et al. High throughput screening tools for thermoelectric materials. J Electron Mater 2015;44 (6):1688–96.

[124] Biswas Kanishka, He Jiaqing, Blum Ivan D, Wu Chun-I, Hogan Timothy P, Seidman David N, Dravid Vinayak P, Kanatzidis Mercouri G. High-performance bulk thermoelectrics with all-scale hierarchical architectures. Nature 2012;489 (7416):414–8.

[125] Curtarolo Stefano, , Gus LW Hart, Marco Buongiorno Nardelli, Mingo Natalio, Sanvito Stefano, Levy Ohad. The high-throughput highway to computational materials design. Nature mat 2013;12(3):191–201.